Applications of Polymer, Composite, and Coating Materials

ZnO-pHEMA Nanocomposites: an Eco-friendly and Reusable Material for Water Remediation

Martina Ussia, Alessandro Di Mauro, Tommaso Mecca, Francesca Cunsolo, Pierfrancesco Cerruti, Giuseppe Nicotra, Corrado Spinella, Giuliana Impellizzeri, Vittorio Privitera, and Sabrina Carola Carroccio

ACS Appl. Mater. Interfaces, **Just Accepted Manuscript** • DOI: 10.1021/acsami.8b13029 • Publication Date (Web): 25 Oct 2018

ZnO-pHEMA Nanocomposites: an Eco-friendly and Reusable Material for Water Remediation

Martina Ussia [a,b], Alessandro Di Mauro*[a], Tommaso Mecca[c], Francesca Cunsolo[c], Giuseppe Nicotra[e], Corrado Spinella[e], Pierfrancesco Cerruti[f], Giuliana Impellizzeri[a], Vittorio Privitera[a], Sabrina C. Carroccio[a,d]

[a] CNR-IMM, Via Santa Sofia 64, 95123, Catania, Italy.

[b] Department of Physics and Astronomy, University of Catania, via Santa Sofia 64, 95123, Catania, Italy.

[c]CNR-ICB, Via Paolo Gaifami 18, 95126, Catania, Italy.

[d]CNR-IPCB, Via Paolo Gaifami 18, 95126, Catania, Italy.

[e] CNR- IMM, Z.I. VIII Strada 5, 95121 Catania, Italy

[f] CNR-IPCB, Via Campi Flegrei 34, 80078 Pozzuoli (NA)

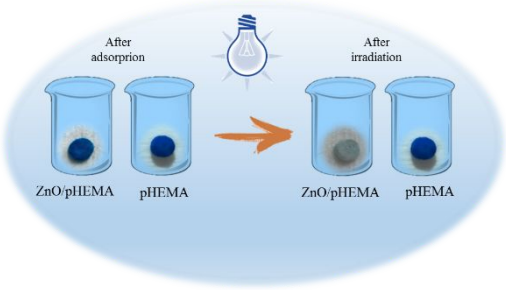

Key words: polymeric adsorbents, cryogel, GO, pHEMA, ZnO, ALD, water remediation, photo-catalysis.

Abstract

The design of new hybrid nanocomposites based on poly (2-hydroxyethylmethacrylate) (pHEMA) graphene oxide (GO) cryo-sponges, wherein ZnO nanolayers have been deposited to induce photocatalytic properties, is here reported. Atomic layer deposition (ALD) at low temperature is specifically selected as deposition technique to stably anchor ZnO molecules to the pendant polymer OH groups. Furthermore, to boost the pHEMA cryo-gel adsorption capability versus organic dyes, GO is added during the synthetic procedure. The morphology, the crystallinity, and the chemical composition of the samples are deeply investigated by scanning electron microscopy (SEM), Transmission electron

microscopy (TEM), X-ray diffraction analyses (XRD), Fourier transform infrared spectroscopy (FTIR) as well as thermogravimetric analysis (TGA). Swelling properties, mechanical performance and adsorption kinetics models of the hybrid materials are also evaluated. Finally, the adsorption and photocatalytic performance are tested and compared for all the samples by using methylene blue (MB) as dye. Particularly, the adsorption efficiency of ZnO/pHEMA and ZnO/pHEMA-GO nanocomposites, as well as their *in situ* regeneration *via* photocatalysis, render such devices very appealing for advanced wastewater treatment technology.

Introduction

Due to rapid population growth and intensification of agricultural and industrial activities, a diverse array of hazardous pollutants is progressively entering in the aquatic system, posing a great threat to human health [1]. The current water purification methods are unable to meet the present needs; many of the procedures used today, including sedimentation, filtration, chemical methods and reverse osmosis, were already established in the beginning of the twentieth century failing to satisfy many requirements. Furthermore, they involve high operating costs and could generate toxic secondary pollutants into the ecosystem[2].

From the technology point of view, adsorption methods hold many advantages being one of the most feasible, efficient as well as low-cost approaches. Various adsorbents, such as carbon-based materials[3,4], clay[5,6], natural and synthetic polymers[7-9], and organic–inorganic composites[10], can selectively capture water pollutants. Among them, super-absorbent polymers have been extensively studied and applied in waste-water treatment [7-9,11,12]. Even though adsorption can efficiently remove pollutants from water, this process presents a critical issue: whatever the adsorbing phase is, it is not able to eliminate in a permanent way the adsorbed pollutants. Therefore, further disposal is required[13]. An eco-friendly and definitive approach to degrade contaminants through their complete mineralization exploits the photo-catalytic

process[14,15]. The latter is considered as one of the most promising and green strategy to improve the quality of water available for use in our daily life. In this context, photocatalysis by using inorganic (TiO_2 and ZnO)[16-26] and organic (photosensitizers and photoactive polymers)[19, 27-28] materials have attracted huge attention, stimulating several synthetic strategies with the aim to boost photocatalytic and visible-light active performances[20, 29-30].

By now, the major barrier prevening the use of such kind of photo-catalysts is their post recovery after water treatment. In fact, the nanoparticles are applied in a slurry to obtain high volumetric generation rate of Reactive Oxygen Species (ROS). At the end of the process, catalysts separation is needed. If nanoparticles are not removed, they can exhibit serious toxicity in aquatic and human life [31]. With this in mind, researchers have been drawing the attention to a practical and safe application of such kind of nanomaterials by using polymers to support them [19,32,33].

In the last decade, the scientific community who works in the field of water purification, has been impressively influenced by the discovery of graphene and its derivatives [34, 35]. Among the materials designed for both adsorption and photocatalysis, a key role is reserved to graphene-based polymeric composites. In this context GO, produced by oxidation of graphite, was intensively investigated as an effective low-cost polymeric filler. The peculiar property that makes GO an excellent candidate as constituent of polymeric materials for water treatment consists principally in its high specific surface area, that provides huge adsorption ability versus organic and inorganic contaminants[34-38]. Furthermore, GO can improve thermal and mechanical stability, and add radical scavenger properties to the blended polymer, allowing enhanced resilience during the recycle steps[39-43]. These properties might constitute also fundamental requirements in the case of the polymer-supported photocatalysts.

In this paper, we report the formulation of a novel multifunctional material, combining in a single system both adsorption and photo-degradation processes, fundamental to remove pollutants in a permanent way. We have selected cryo-polymerization in water as a green method to produce sponges[41-44], eventually

adding GO during the non-frozen phase. As known, cryo-gelation allows preparing porous gels with high toughness and superfast responsivity. In the last 15 years, due to their extraordinary properties, cryogels have attracted intense attention resulting in several biotechnological and biomedical areas[44, 45]. Here, we explore their application in the water remediation field. With this aim, the synthesis of ad hoc super-adsorbent polymeric composite was performed by using 2-hydroxyethyl methacrylate (HEMA) as monomer and GO as filler.

Notably, taking advantage from the hydroxyl pendant groups on HEMA moieties, our strategy also involves the covalent linkage of HEMA to the ZnO molecules by using atomic layer deposition (ALD) [46,47]. The use of ZnO, through a stable covalent linkage between the polymeric support and the photocatalyst, provides a freestanding material, easily and safely removable from the polluted site and able to degrade pollutants after each adsorption step as well. This represents a crucial advantage. Indeed, nicely adsorbent devices reported in the recent literature, present excellent performance in terms of dyes removal, even if their regeneration is still challenging[48,49].

The formulated multifunctional polymer nanocomposites were characterized by Fourier transform infrared (FTIR) spectroscopy, thermogravimetric analysis (TGA), scanning and transmission electron microscopy (SEM and TEM), and X-ray diffraction (XRD). Their adsorption capability, contact time, mechanical performances, recyclability and photocatalytic efficiency versus MB removal, are here reported and discussed.

Results and discussion

The pHEMA polymeric materials were synthesized *via* cryo-structuration method at a temperature below the water freezing point (see the experimental section). In our synthesis, the polymerization yield ranges from 80-85% for all the samples. GO was added as a filler to impart superior adsorption efficiencies versus anionic and cationic organic dyes [34] and its final content into the polymer composite was estimated

by TGA (see Table 1). Finally, in order to produce a photocatalytic activity, it was further chemically modified by introducing ZnO through ALD (see experimental section). Given that, the cryo-sponges obtained (pHEMA, pHEMA-GO, ZnO/pHEMA, ZnO/pHEMA-GO) were subjected to the morphological and physico-chemical characterizations reported as follows.

SEM and TEM analyses

In Fig. 1 SEM micrographs of all typologies of synthesized samples are reported. The pHEMA samples images (Fig. 1(a-d)), reveal typical structures consisting in microporous jagged surface, with a random 3D network.

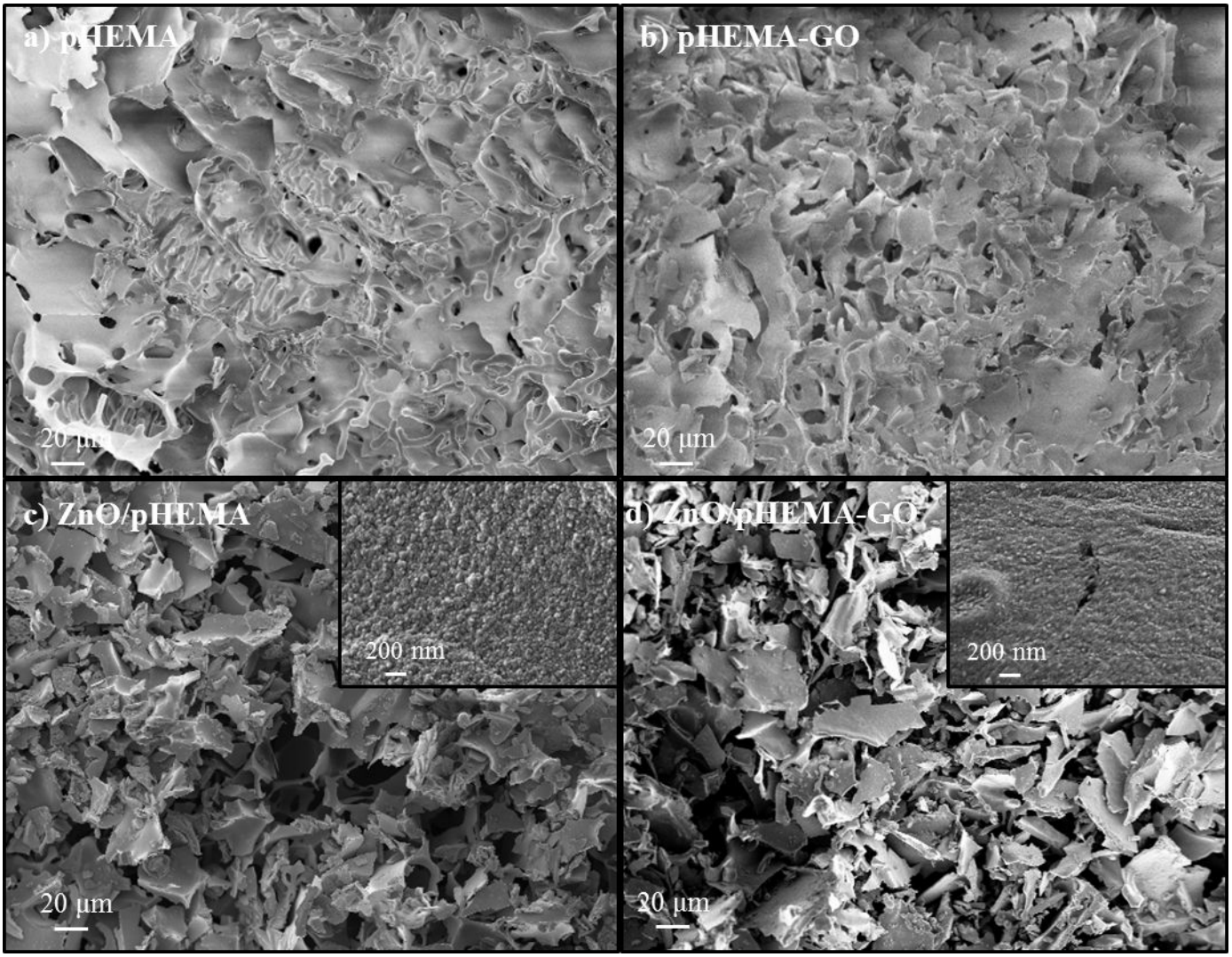

Figure 1. SEM images of pHEMA (a), pHEMA-GO (b), ZnO/pHEMA (c), and ZnO/pHEMA-GO (d), together with high magnification images reported as insets of figures (c) and (d).

Even if the images collected for samples containing ZnO (Fig. 1(c-d)) appear much more resolved, they did not reveal any significant structural modifications if compared to the samples without ZnO. This is likely due to the great conformability of the ALD process[49]. In the insets of Fig. 1, high magnifications of the surfaces of pHEMA and pHEMA-GO coated with ZnO are reported on top. The images displayed the typical morphology of ZnO, formed by small grains, uniformly distributed on the surface, showing a regular shapes and sizes coating[50].

Figure 2 reports the TEM analyses of the ZnO/PHEMA sample. In particular, the TEM image in plan-view (Fig. 2 a) confirms the morphology of the ZnO/pHEMA already showed by the SEM analyses reported in Fig. 1; the ZnO thin film is made of grains with an average diameters of ~ 10 ± 1 nm (calculated by measuring the diameter of several grains, by Digital Micrograph 3.6.1 of Gatan Inc.). The cross-section TEM image reported in Fig. 2 b) shows the great conformality of the ZnO film due to the ALD technique, and indicates a mean film thickness of ~ 15 nm.

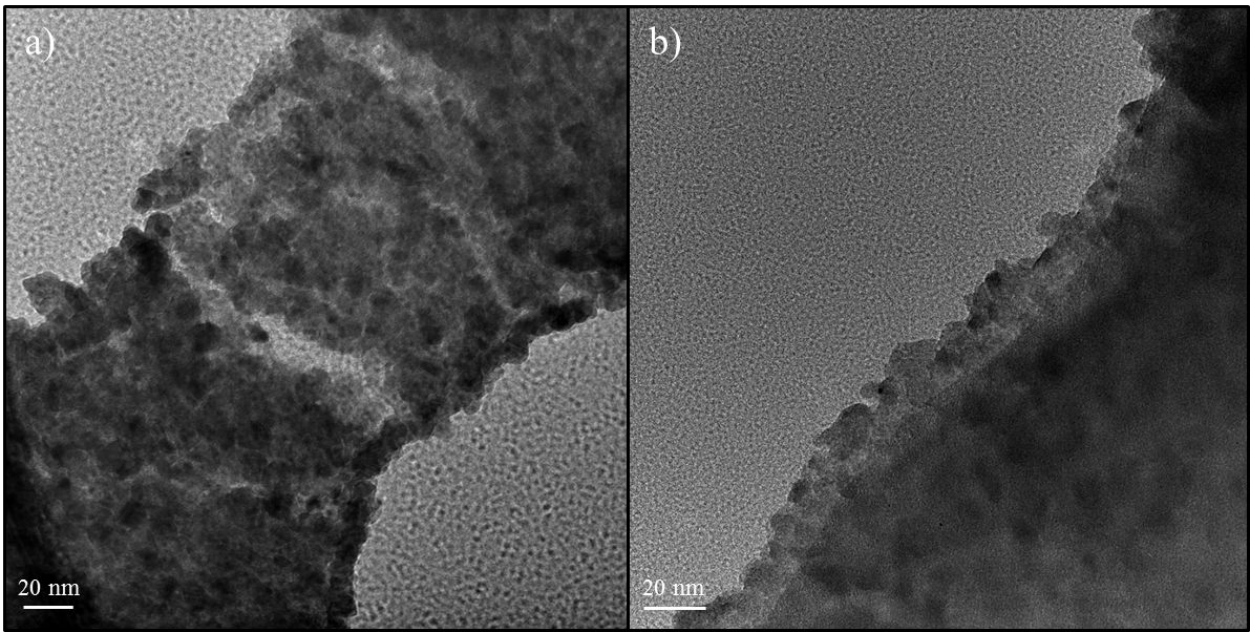

Figure 2. TEM images of plan view (a) and cross section (b).

XRD analysis

To further appreciate the presence of photoactive ZnO crystals on the pHEMA materials, XRD analysis was performed before and after ALD procedure (Figure 3).

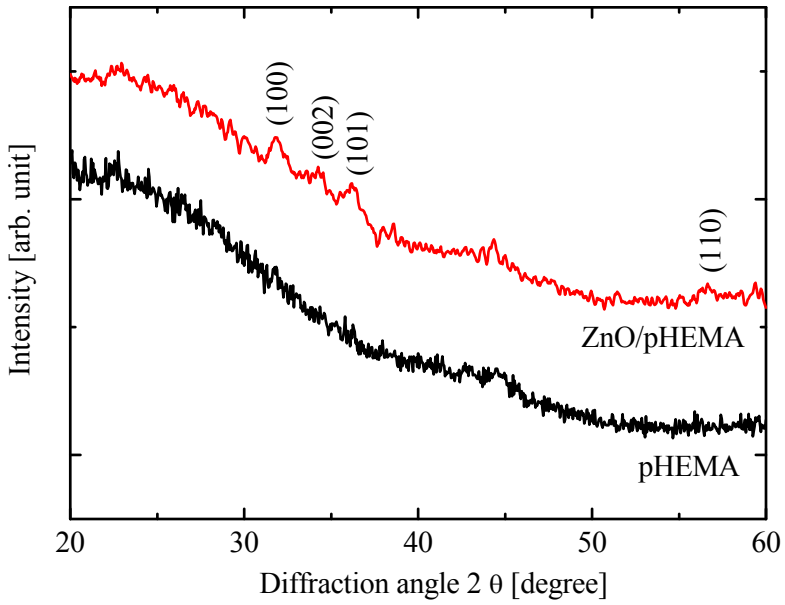

Figure 3. XRD patterns of pHEMA, and ZnO/pHEMA (from the bottom to the top).

The large band observed for the pHEMA in Figure 3 is related to the amorphous structure of the polymer. In particular, patterns for both samples showed very broad features consistent with the incoherent scattering from an amorphous solid. Conversely, after ALD cycles of ZnO, the pattern of ZnO/pHEMA shows well-defined Bragg peaks corresponding to the planes (100), (002), (101), (110), confirming the wurtzite crystal structure of the thin deposited films (JCPDS 36-1451).

The average crystalline size is assumed to be the size of a coherently diffracting domain, and it was calculated from the XRD peak width of (101), based on the Debye–Scherrer equation[51], reported below:

$$D = \frac{k\lambda}{\beta_{hkl}\cos\theta} \qquad (1)$$

where β_{hkl} is the integral half width, k is a constant equal to 0.90, λ is the wavelength of the incident X-ray (λ = 0.1540 nm), D is the crystallite size, and θ is the Bragg angle. The average crystalline size for the ZnO thin film resulted 10 ± 1 nm that is equal to the value calculated by the TEM analyses.

Thermal analysis

In order to quantify the inorganic content into the samples as well as their thermal stability, thermal analysis by using TGA was also performed.

Table 1. Temperature at maximum rate of decomposition and residual masses of pHEMA samples as estimated through TGA analyses.

SAMPLE	T_{MD} [°C]	Residue at T=800°C [wt.%]
PHEMA	425±2	2.8±0.8
PHEMA-GO	426±1	3.4±2.1
ZnO/PHEMA	418±2	10±1.5
ZnO/PHEMA-GO	404±2	14.9±0.8

In Table 1 the results of TGA performed by using N_2 as gas carrier up to 800 °C are summarized. The temperatures at the maximum derivative of weight loss (T_{MD}) range from 404 to 426 °C depending on the material formulation. The low content of GO into the polymer did not significantly change the thermal behaviour of the material, whereas the samples enriched with ZnO nanostructures produce a sensible decrease of T_{MD} of about 8-20 °C with a residue ranging from 10-15% depending on the ZnO samples. Indeed, as reported in the literature for the poly methylmethacrylate (PMMA), a content in ZnO higher than 0.15%, determines lower temperatures of polymer degradation[52]. The TGA results also indicate a 4.9% of residue in ZnO/pHEMA-GO higher than in ZnO/pHEMA sample. This finding is more likely attributed to the presence of ≅ 0.6% of GO into the polymer specimen. As reported in the experimental section, GO is constituted of aggregates containing 15-20 sheets with a 4-10 % of edge-oxidized. We reasonably suppose that ZnO nucleated on the defect sites, reacting with the oxidised groups in a covalent

mode, contributing to its increment into the final material[53]. For more details, the TGA and DTGA (derivate of TG) curves are reported in the supplementary information (Figs S1-S4).

Swelling Test

High absorption capacity, quick absorption equilibrium and/or swelling−deswelling properties are fundamental parameters that have to be estimated, in order to establish the capture efficiency of the formulated materials versus organic pollutants in water.

The dynamic adsorption behaviour of the prepared ZnO and GO samples was tested and compared with the pHEMA reference[11, 54-56]. The equilibrium swelling degree can be calculated using the following formula[57].

$$swelling\ degree = \frac{(m_w - m_d)}{m_d} \qquad (2)$$

where m_w is the weight of the wet cryogel and m_d is the weight of the dry cryogel.

In Fig. 4, the equilibrium swelling degree (ESD) for each sample is reported. The column graph shows similar ESD values for pHEMA, ZnO/pHEMA, and pHEMA-GO: ~ 9.5 ± 0.2 g/g, while a lower value was measured for ZnO/pHEMA-GO: ~ 6.0 ± 0.2 g/g. This clearly means that the ZnO/pHEMA-GO samples is able to adsorb a smaller amount of water. This result is supported by TGA analyses, that reveal an higher content of ZnO in ZnO/pHEMA-GO if compared with ZnO/pHEMA samples, and consistent with data reported in the literature indicating a not relevant water adsorption for ZnO films[52]; as a consequence, higher ZnO content would induce a lower swelling capacity.

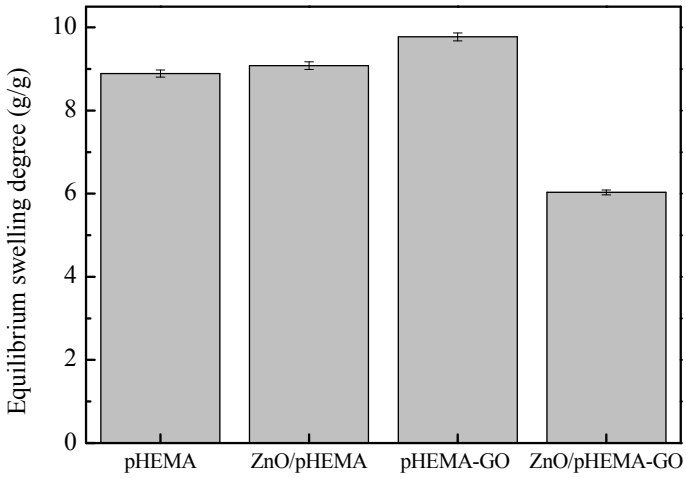

Figure 4. Equilibrium swelling degree of pHEMA, ZnO/pHEMA, pHEMA-GO, and ZnO/pHEMA-GO.

Figure 5 reports the normalized swelling degrees in water as a function of time. All the samples took only 2.5 s to reach ~ 95% of the equilibrium swelling capacity, achieving the equilibrium-swollen state in less than 10 s. In this case, the presence of the ZnO into the material formulations did not influence in a relevant manner the swelling rate of the composites. Furthermore, the ZnO nanocomposites exhibit superfast and stable oscillatory swelling−deswelling up to 5 cycles (Fig. 6) without any significant loss in the swelling degree and water recovery, similar to the results reported by Wang et al. in the literature[12]. Although the swelling performance of ZnO/pHEMA-GO samples reported in Fig.s 4 and 6 appears to be slightly affected by the higher amount of the ZnO (see Table 1), we suppose that its contribution certainly could make the difference in terms of pollutants removal.

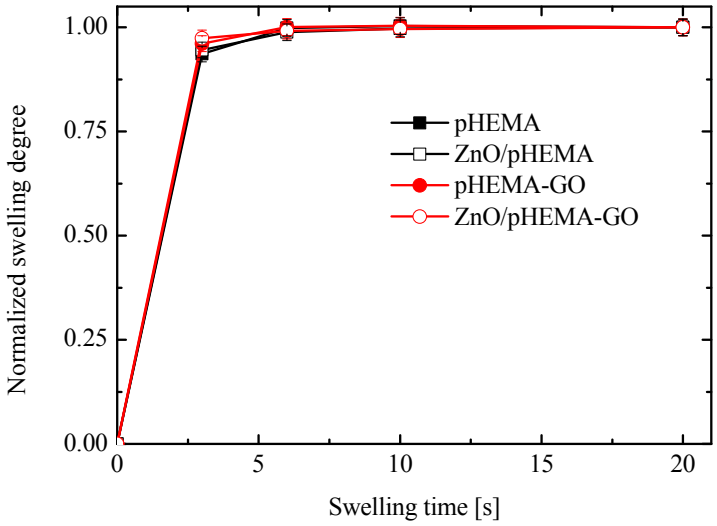

Figure 5. Dynamic swelling profiles of pHEMA, ZnO/pHEMA, pHEMA-GO, and ZnO/pHEMA-GO.

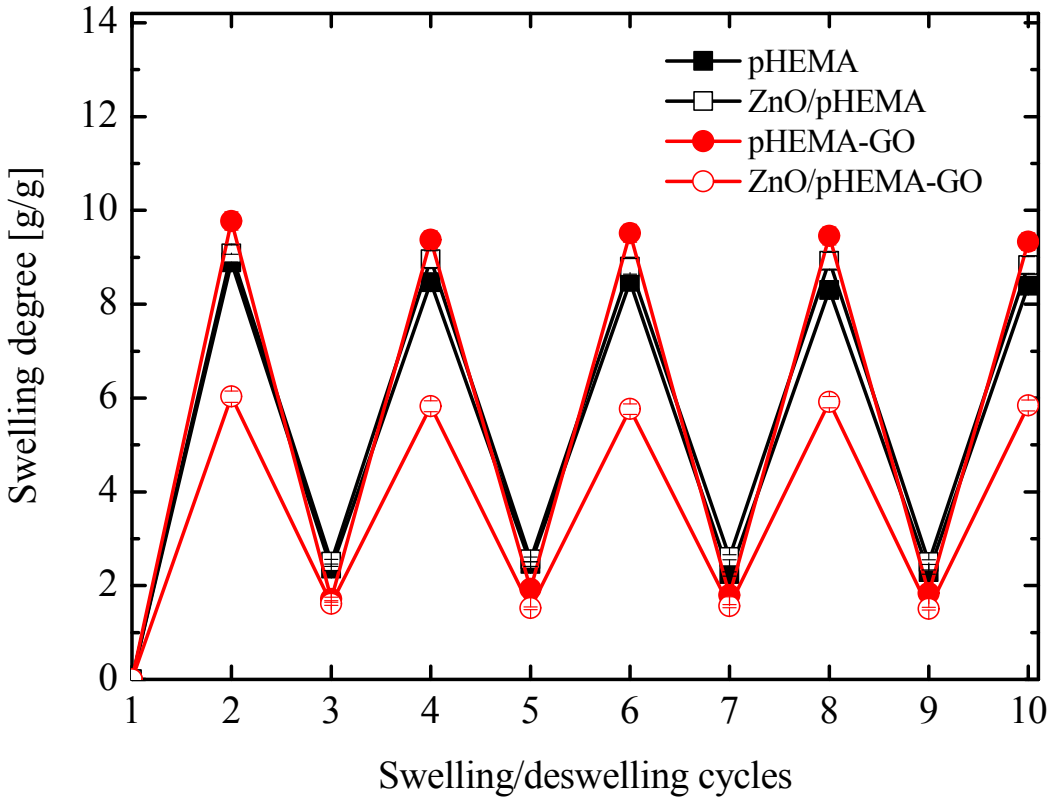

Figure 6. Swelling/ deswelling degree cycles of all pHEMA samples

The porosity of the dried samples was calculated as percentage by measuring the absorbed volume of cyclohexane versus the total volume of each sample (see experimental section). The data displayed in Figure 7 evidenced as the porosity of pHEMA was not altered by the addition of GO, as well as of ZnO molecules. In particular, ZnO nano-structuration by ALD could determine the shrinkage of the pores size, affecting the final access to the surrounding medium. Our results (Fig. 7) do not show any significant differences in cyclohexane uptake for all samples, suggesting that any shrinkage of pores size occurs after ZnO deposition.

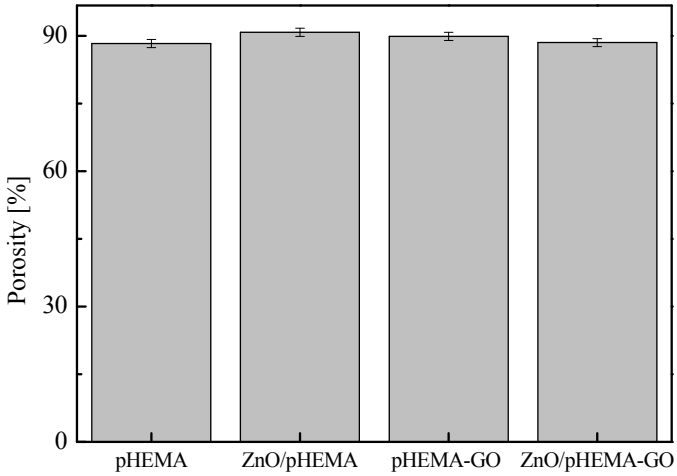

Figure 7. Porosity of pHEMA, ZnO/pHEMA, pHEMA-GO, and ZnO/pHEMA-GO cryogels.

Mechanical characterization

The curves displaying the stress-strain behavior of the cryogels subjected to compression tests are shown in Figure 8.

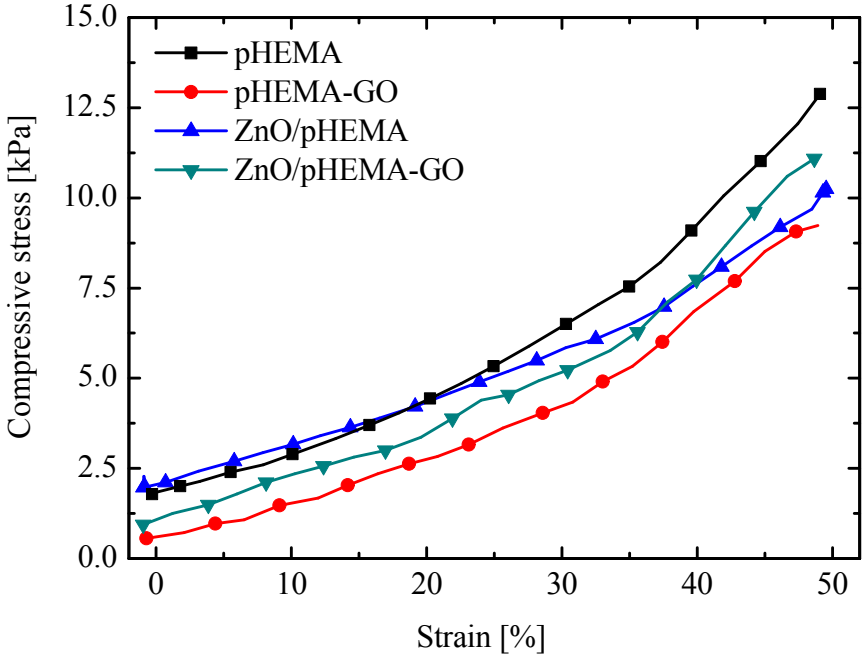

Figure 8. Stress-strain curves of pHEMA, ZnO/pHEMA, pHEMA-GO, and ZnO/pHEMA-GO wet cryogels subjected to compression test.

All the samples could bear compression strain of 50% without permanent deformation or mechanical destruction. As expected, all the curves exhibited an elastic deformation region at low strain values followed by a non-linear stage at compression values above 30%[58]. It is noticed that pHEMA-GO displayed slightly lower values of compressive stress all over the deformation range investigated, likely due to its higher equilibrium swelling degree.

In addition this can also arise from a slightly lower crosslinking density due to the interference of GO during the polymerization step. ZnO deposition on pHEMA-GO resulted in increased compression stress, while ZnO/pHEMA did not show significant differences in comparison with pHEMA. The Young's modulus values calculated from the elastic region (< 20% strain) were found to be 12.5 ± 1.8 kPa (pHEMA), 10.9 ± 0.5 kPa (pHEMA-GO), 10.7 ± 2.1 kPa (ZnO/pHEMA) and 11.7 ± 1.0 kPa

(ZnO/pHEMA-GO). These values are comparable with those reported for other HEMA based cryogels[59], and demonstrate the though and elastic nature of the cryogels which is appropriate for the envisaged application.

In order to get insight into the recyclability of the cryogels, 10-cycle compression tests were carried out, which provided information on the mechanical stability of the samples (Figure S5). All the samples showed very good mechanical reversibility upon compression cycling, as after 10 cycles at 50% strain the cryogels maintained 97.3% (pHEMA), 87.2% (pHEMA-GO), 92.8% (ZnO/pHEMA), and 88.0% (ZnO/pHEMA-GO) of the initial compression stress.

Kinetic adsorption studies

Kinetic adsorption studies were carried out at room temperature to provide information concerning the interaction mechanisms that occur between dye and our functionalized pHEMA materials.

In order to evaluate the amount of MB adsorbed at equilibrium, the cryogels were immersed in a solution of MB overnight, until the equilibrium was reached. At time *t,* the adsorption capacity Q_t (mg g $^{-1}$), was determined by the following equation[60]:

$$Q_t = \frac{(C_0 - C_t)V}{W} \qquad (3)$$

Where C_0 (mg L^{-1}) is the initial concentration of MB, C_t (mg L^{-1}) is the concentration of MB at time *t*, *V* (L) is the volume of the solvent, *W* (g) is the amount of adsorbent used in the adsorption process. The results of this experiment are reported in Fig. 9.

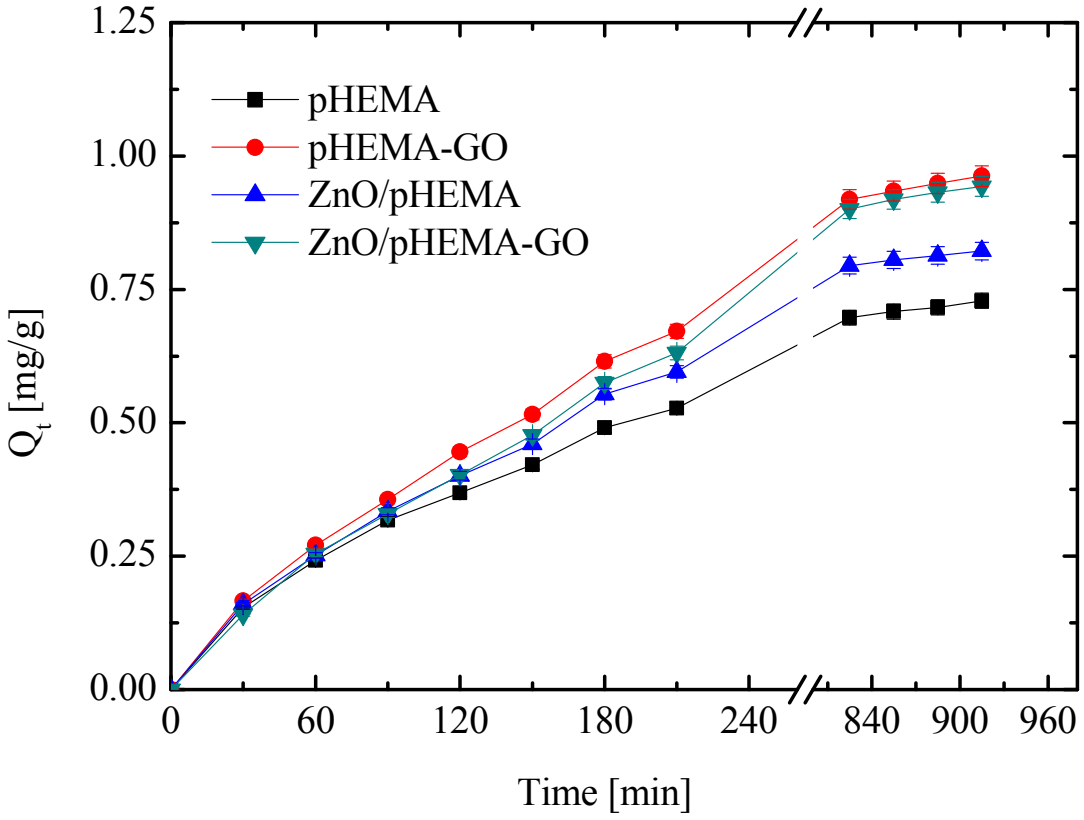

Figure 9. MB adsorption capacity versus time for pHEMA, pHEMA-GO, ZnO/pHEMA, and ZnO/pHEMA-GO.

To further achieve information on distribution of MB molecules between the solid and liquid phase at the equilibrium, the adsorption kinetics and the capacity of the cryogels at the equilibrium were monitored by using the adsorption isotherms. The adsorption capacity at the equilibrium, Q_e (mg g^{-1}), was computed by the following equation:

$$Q_e = \frac{(C_0 - C_e) \times V}{W} \qquad (4)$$

where C_0 (mg L^{-1}) is the initial concentration of MB, C_e (mg L^{-1}) is the concentration of MB at the equilibrium, V (L) is the volume of the solution, W (g) is the amount of adsorbent used in the adsorption process.

In Table 2 the values of Q_e for each sample were reported. As predictable, the samples containing GO (pHEMA-GO and ZnO/pHEMA-GO), exhibited higher adsorption capacities if compared to the unfilled GO samples [31].

Table 2. Equilibrium adsorption capacity of the tested cryogels at room temperature.

SAMPLE	Q_e [mg/g]
pHEMA	0.73 ± 0.01
pHEMA-GO	0.97± 0.02
ZnO/pHEMA	0.82±0.02
ZnO/pHEMA-GO	0.94±0.02

Adsorption reaction models are widely utilized to describe and discriminate among the different kinetic process of adsorption phenomenon. In static conditions the most applied models are the pseudo-first-order, pseudo-second-order, and intraparticle diffusion[61,62]. The pseudo-first-order model presented by Lagergren is based on the solids capacity to adsorb and is given by Eq. (5)[63]:

$$\frac{dQ_t}{dt} = k_1(Q_e - Q_t) \qquad (5)$$

where Q_e and Q_t (mg g $^{-1}$) are the adsorption capacities at equilibrium and time t (min), respectively, and k_1 (min^{-1}) is the pseudo-first-order rate constant of the kinetic model. Integrating Eq. (4) using the initial conditions of $Q_t = 0$ at $t = 0$ leads to Eq. (6) [60]

$$\ln\left(\frac{Q_e}{Q_e - Q_t}\right) = k_1 t \qquad (6)$$

which can be rewritten as

$$\ln\left(Q_e - Q_t\right) = \ln Q_e - k_1 t \qquad (7)$$

This model is normally used when the adsorption operation is fast, attaining the equilibrium within 20–30 min.

In the second-order model the driving force (Q_e-Q_t) is proportional to the available fraction of active sites, and it can be written as:

$$\frac{dQ_t}{dt} = k_2(Q_e - Q_t)^2 \qquad (8)$$

and integrating Eq. (8)

$$\frac{1}{(Q_e - Q_t)} = \frac{1}{Q_e} + k_2 t \qquad (9)$$

This last equation can be rewritten as follows:

$$\frac{t}{Q_t} = \frac{1}{k_2 Q_e^2} + \frac{t}{Q_e} \qquad (10)$$

The second-order rate equation has been successfully applied to the adsorption of metal ions, dyes, and organic substances from aqueous solutions. Several studies for adsorption of divalent metals reported that the majority of the sorption kinetics follows pseudo-second-order mechanism[64,65].

A functional relationship common to most of the treatments of intraparticle diffusion is that uptake varies almost proportionately with the half-power of time ($t^{0.5}$), rather than t. Good linearization of the data is observed for the initial phase of the reaction in accordance with the expected behaviour if intraparticle diffusion is the rate-limiting step[66].

The intraparticle diffusion model is expressed by the following equation:

$$Q_t = k_i\sqrt{t} + C \qquad (11)$$

where k_i is the intraparticle diffusion rate constant (mg $g^{-1}h^{-0.5}$).

The k_i values are calculated from the slope of the straight line of the respective plots. The plot of Q_t versus $t^{0.5}$ may present multi-linearity, which indicates that two or more rate controlling steps occur in the adsorption process.

Based on three discussed models, several fittings of the experimental data were performed. In Table 3 the values of R^2 for all samples are reported. The comparison of R^2 for the three different models clearly shows that our experimental data fit more closely to the pseudo-second-order law (Figure 10).

Table 3. R^2 values for the different kinetic models of MB adsorption on the tested samples.

R^2	I Order	II order	Intraparticle diffusion
pHEMA	0.929	0.999	0.923
pHEMA-GO	0.917	0.998	0.912
pHEMA/ZnO	0.918	0.998	0.928
pHEMA-GO/ZnO	0.814	0.997	0.956

As reported in the literature[68], the pseudo-second-order kinetic model assumes that a chemisorption process occurs. As desirable, we can conclude that the MB adsorption performed by our pHEMA cryogels is mainly driven by chemical interactions.

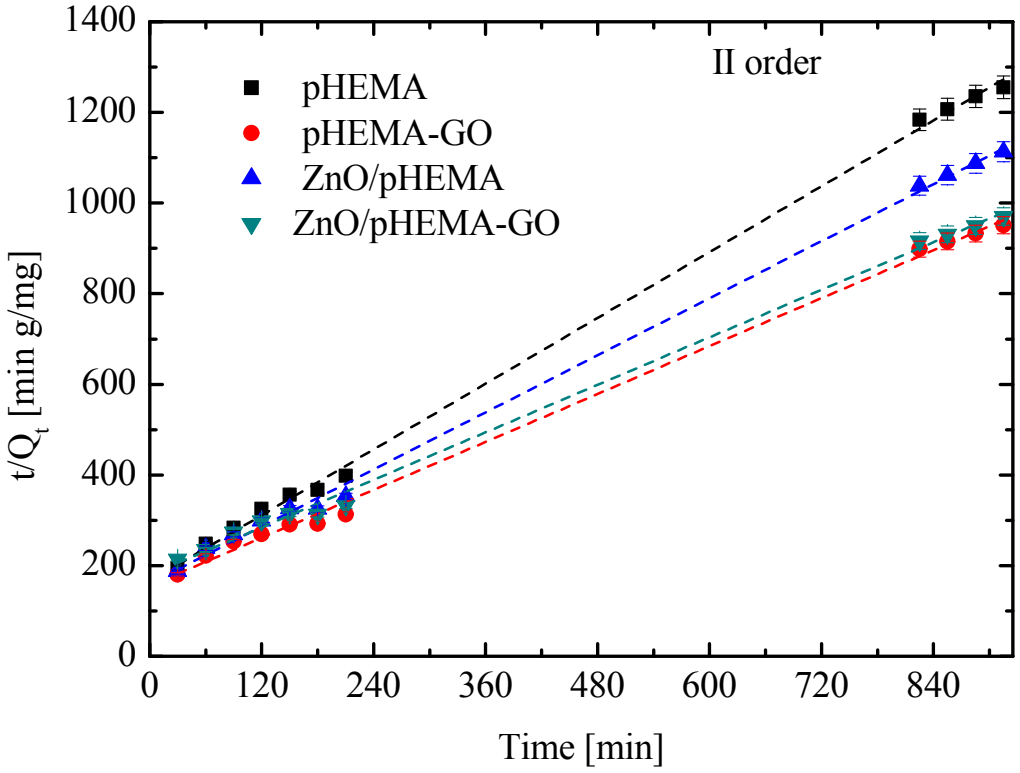

Figure 10. Adsorption kinetic of MB for pHEMA (squares), pHEMA-GO (circles), ZnO/pHEMA (up triangles), and ZnO/pHEMA-GO (down triangles) fitted with the pseudo-second-order model (dashed lines).

Adsorption/photocatalytic test

To verify the efficacy of the regeneration process accomplished by the ZnO polymer coating, adsorption followed by photocatalytic process for all the samples was executed by using MB solution as organic pollutant reference. Three adsorption processes were performed; between them, all samples were irradiated by an UV lamp to regenerate the material *via* the photocatalytic action of ZnO.

The adsorption results collected in each cycle (420 min for each cycle) were summarized in Fig. 11, reporting a column graph with the percentage of adsorbed amount of MB for the different samples. The MB dye adsorption was performed in the absence of adsorbent materials, in the presence of pHEMA,

pHEMA-GO, ZnO/pHEMA, and ZnO/pHEMA-GO. As expected, no variations in adsorbance percentage values were revealed in the MB reference experiment. During the first cycle, pHEMA adsorbs ~37% of MB, while pHEMA-GO is able to adsorb ~ 57% of the dye. The higher value obtained from the latter sample is due to the excellent capability of GO to capture pollutants[32]. ZnO/pHEMA and ZnO/pHEMA-GO samples absorb ~ 41% of MB (see Fig. 11). This finding can be reasonable ascribed to the ZnO coverage of the GO sheets that, hindering the interactions between dye molecules and GO surface, decrease the peculiar GO sequester performance. After the second and third cycles, pHEMA and pHEMA-GO exhibit a sensible decrease in the adsorption capacity, indicating that the merely UV exposure was not able to photodegrade the adsorbed MB. Consequently, the materials after the 3rd adsorption cycle were not regenerated. As evidenced in the figure, the values decrease from the first to the third cycle in both pHEMA and pHEMA-GO up to ~ 22%, and ~ 35%, respectively. Differently, the corresponding samples coated with ZnO showed a nicely comparable adsorption capacity during the three cycles, proving as these devices can be efficiently regenerated by UV light irradiation. Figure S6 reports the evolution time up to 420 min of the MB residual concentration during the adsorption processes for the three cycles. The anchorage of the photocatalyst to the polymeric sponges, that is able to produce ROS in water, clearly play a decisive role in this experiment.

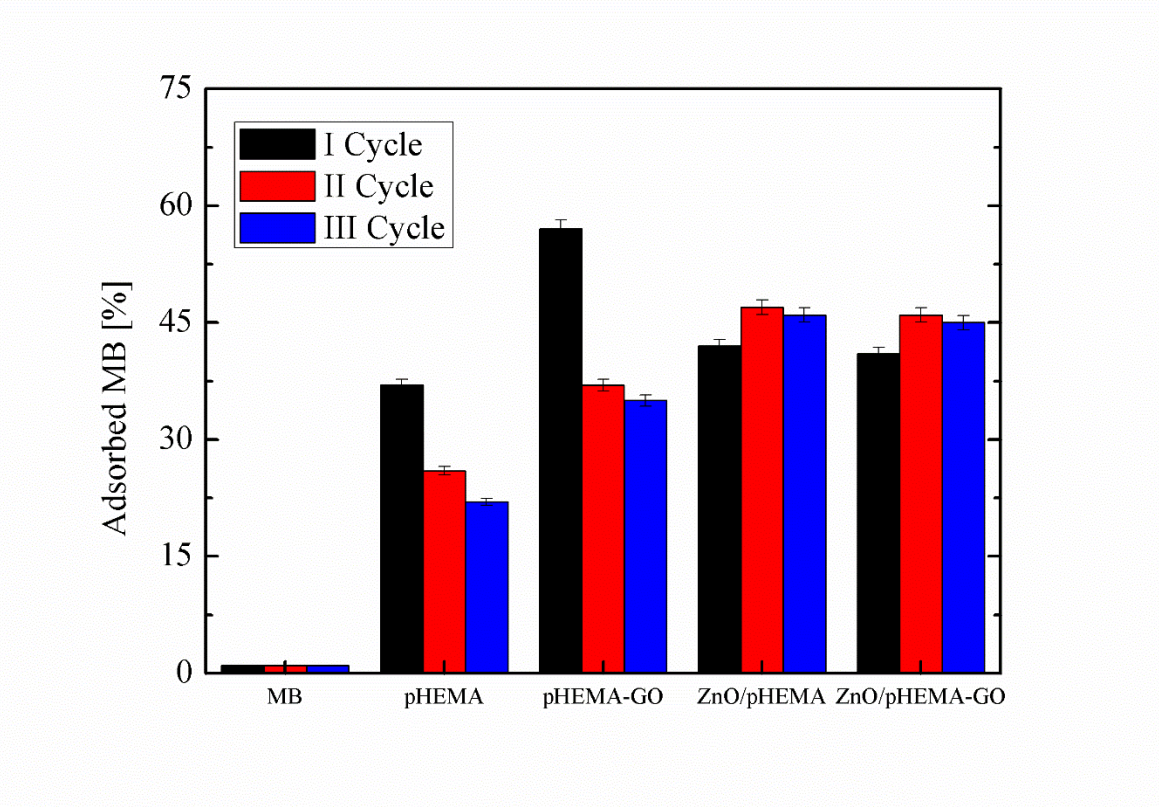

Figure 11. Recyclability after three adsorption cycles of MB, pHEMA, pHEMA GO, ZnO/pHEMA and ZnO/pHEMA-GO.

To corroborate the effective photo removal of MB after UV light exposure, FTIR analyses were performed of the pHEMA and ZnO/pHEMA samples. Fig. 12 shows the spectra of pHEMA as-prepared (the first from the top), after the first cycle of the adsorption process (the second from the top), and, after the photocatalytic process (the third from the top). The pHEMA diagnostic bands at 3400-3100, 2895-2854, 1722, 1162 and 1022 cm^{-1}, corresponding to O-H, C-H, C=O, C-C-O group stretching vibrations, and O-H bending, respectively appeared in the IR profile[68]. The FTIR spectrum of MB in Fig. 11 reported as reference, clearly showed the typical peaks of the dye. In particular, the peak at 1600 cm^{-1} related to the C=C stretching of aromatic ring and the two peaks at 1354, and 1340 cm^{-1}, associated with two different C-N bonds of MB (see vertical dashed lines in Fig. 12)[69]. As expected, after MB adsorption, the IR spectra of both pHEMA and ZnO/pHEMA revealed the appearance of aforementioned MB peaks

(drawn lines) among the signals, while, from the inspection of the identical samples subjected to the UV irradiation up to 5 hrs, their disappearance was evident. Accordingly, in the IR spectra of irradiated virgin pHEMA, peaks belonging to MB remained visible.

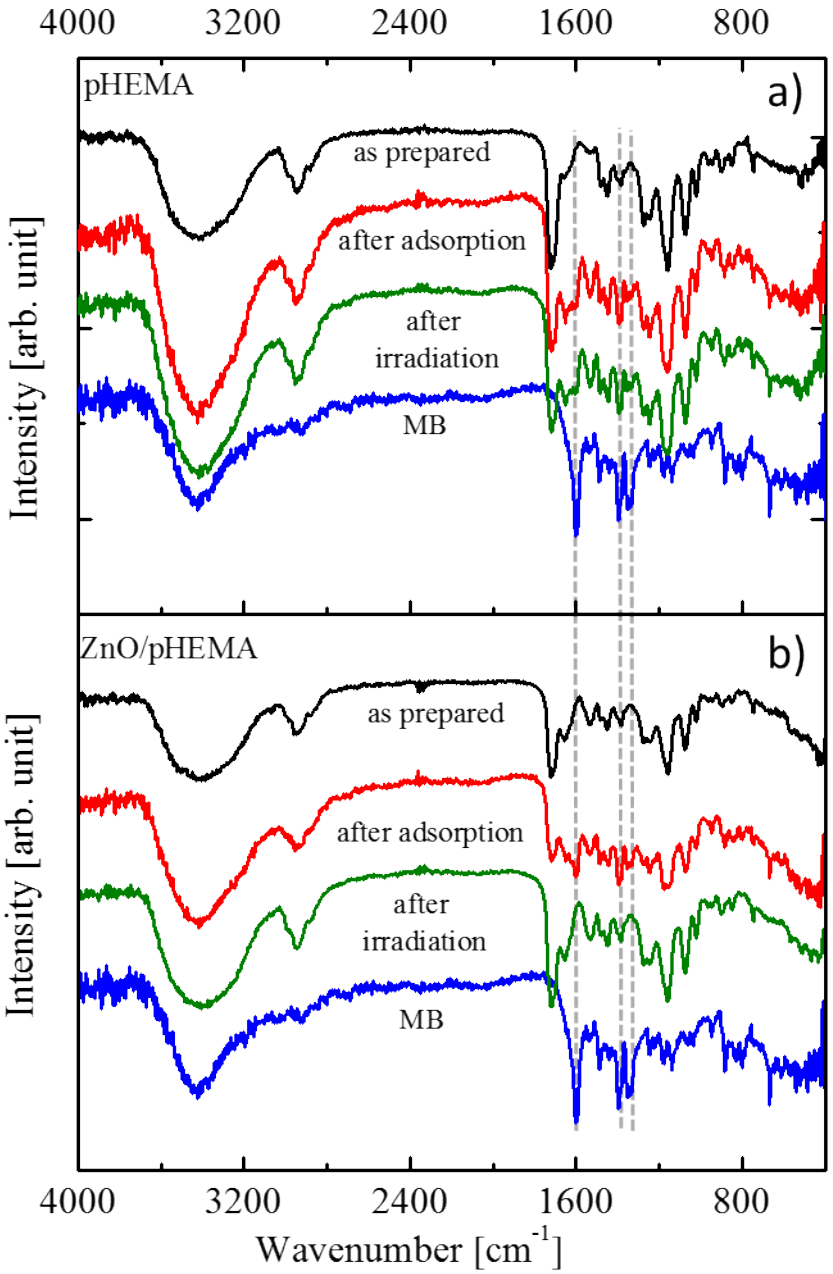

Figure 12. FTIR spectra measured on pHEMA (a), and on ZnO/pHEMA (b), as prepared (first spectrum from the top), after MB adsorption (second spectrum from the top), and after regeneration by UV light irradiation. The spectrum of pure MB is shown as reference. The spectra were vertically shifted for clarity. Vertical dashed lines indicate the typical stretching peaks of MB.

FTIR analysis of ZnO/pHEMA-GO sample was also performed, showing a similar trend (S7). To verify the chemical stability of the samples after the regeneration by the photocatalytic process SEM and XRD analyses of ZnO/pHEMA after the regeneration have been performed and reported in Fig. 13 (a-b). In particular, SEM images (Fig. 13 a) show the same morphology of the ZnO/pHEMA before the adsorption process (Fig. 1). The diffractogram of ZnO/pHEMA after the photo-regeneration (Fig. 13 b) presents the peaks related to the wurtzite structure at 31.8 °, 34.5° and 36.5°. The grain size, calculated by the Scherrer's law, resulted 10 ± 1 nm, not showing any substantial variation with respect to the size calculated before the photocatalytic regeneration.

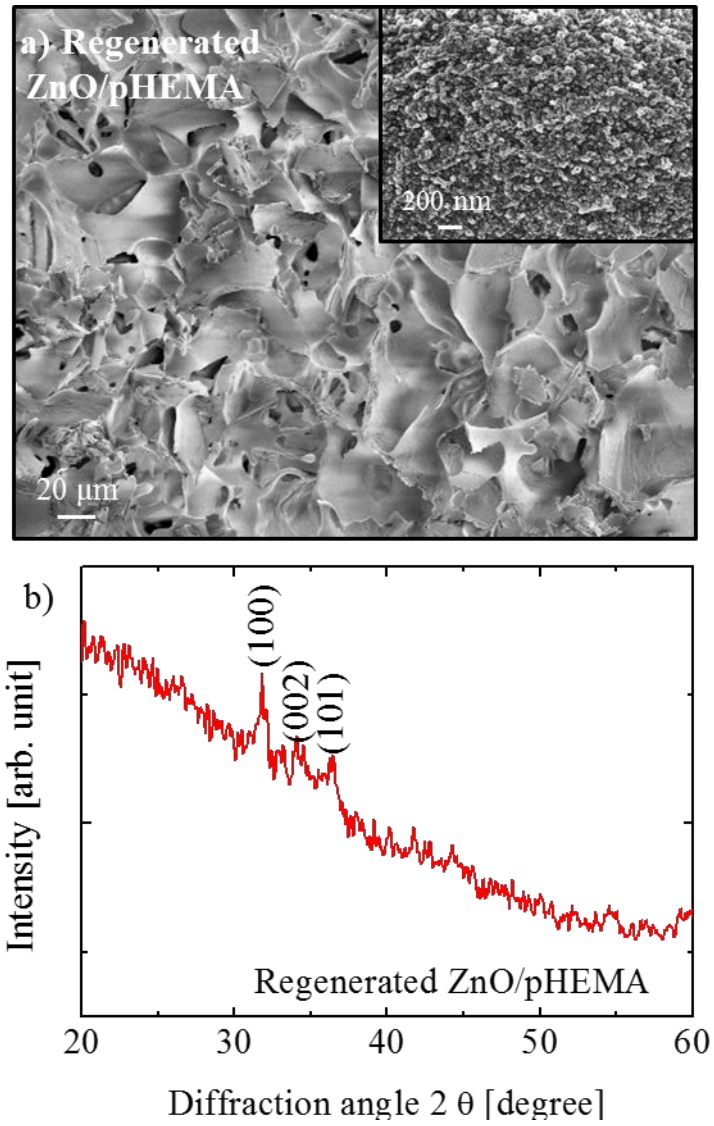

Figure 13. a) SEM analysis of ZnO/pHEMAafter the regeneration, and high magnification (inset); b) XRD diffractogram of the regenerated ZnO/pHEMA.

Experimental Section

Materials

2-hydroxyethylmethacrylate (HEMA), N,N-methylenebisacrylamide(MBAA), ammonium persulfate (APS), N,N,N',N'-tetramethylethylenediamine (TEMED) and graphene oxide (GO) in water solution 1mg/mL containing aggregates of 15-20 sheets with a 4-10 % of edge-oxidized were purchased from Sigma Aldrich.

Preparation of pHEMA and pHEMA-GO

The pHEMA cryogel was obtained following the described procedure previously [70], using 10% w/w monomers (HEMA and MBAA) solution in water with a molar ratio of 6:1, HEMA:MBAA, and 1% w/w APS/TEMED of the total monomers. Each cryogel was synthesized in 0.5 mL solution in a glass tube, 6 mm in diameter, and frozen overnight at -16 °C. The cryogels were then washed with water, ethanol and diethyl-ether and left to dry at room temperature under nitrogen flux. At this stage, the unmodified pHEMA cryogel represents the plain cryogel used as a reference. To obtain the GO cryo-composite, a sonicated 0.2 % water solution of GO was used as medium to synthetize HEMA and then treated as reported above. The samples used for ALD, TGA and photocatalytic experiments, were cut in pieces of 0.4 cm using the same section eliminating the top and the bottom part of the specimens.

Atomic layer deposition of ZnO on pHEMA and pHEMA-GO

ZnO films were deposited by ALD using the Picosun R-200 Advanced reactor. During the deposition the temperature was fixed at 80 °C. The ZnO was deposited on cylinders of pHEMA, pHEMA-GO, and in pieces of silicon as reference. Diethyl zinc (DEZ, purity 99.9999%) and de-ionized water were used as precursors, while N_2 was used as carrier and purge gas (purity ≥ 99.999%). The pulse and purge time were kept constant at 0.1/3/0.1/5 s for DEZ/N_2/H_2O/N_2, by using three-times pulses for both DEZ and H_2O precursor, for a total of 110 cycles. The flow rate for DEZ and H_2O were 150 sccm and 200 sccm, respectively, while the flow in the other lines was 40 sccm. The pressure of the reactor was ~ 10 hPa. The precursor's temperatures were fixed at 22 °C. The film thickness was evaluated thanks to ZnO deposited on silicon, by the Woollam M-2000 spectroscopic ellipsometer, by applying a Cauchy model in the 400–1700 nm range. The film thickness resulted ~ 15 nm. The pHEMA, and pHEMA-GO used

for this study had a weight of ~ 5 mg. The synthesized materials after the ZnO deposition will be hereafter called: "ZnO/pHEMA" and "ZnO/pHEMA-GO

Characterization

All the synthesized materials were deeply characterized. The morphology of the sponges were investigated by SEM, with a field emission Zeiss Supra 25 microscope. The pHEMA and ZnO/pHEMA samples, were previously coated, by sputtering, with a 10 nm thick gold film, in order to prevent electron beam charging of the insulating polymer.

TEM analyses were performed with a JEOL ARM200F Cs-corrected operated at low current and low voltage, 60keV, in order to avoid specimen damaging and charging. All the images have been acquired in Conventional TEM (C/TEM) mode and Bright Field (BF). Inelastic scattering contribution of the electrons has been removed by inserting the energy filter, a GATAN Quantum ER, with a 10eV energy slit tuned on zero loss in order to improve the contrast and better localize the nanoparticles.

As for the specimen preparation, the processed specimen has been gently scratched on an ultra thin Carbon TEM grid, and transferred to the microscope.

The structure of the samples was evaluated by XRD analyses, with a Bruker D-500 diffractometer, operating with a parallel Cu-Kα radiation at 40 kV and 40 mA, 2θ from 20° to 60°, in θ /2θ mode. The XRD spectra were analysed by the Bruker software suite, including ICSD structure database.

The thermogravimetric analyses of the samples were performed using a thermogravimetric apparatus (TGA, TA Instruments Q500) under nitrogen atmosphere (flow rate 60 mL/min) at 10 °C/min heating rate, from 40 °C to 800 °C. Sample weights were approximately 6 mg. TGA sensitivity is 0.1µg with a weighting precision of ± 0.01%. The isothermal temperature accuracy is ± 1°C.

The swelling properties were determined by gravimetric analyses. For the determination of the swelling profile, dried samples in the form of cylinders, ~5 mm in diameter and 4 mm in height, were

swollen in de-ionized water. Excess of surface water was gently wiped off using filter papers before any measurements of the mass of the swollen sample.

To calculate the equilibrium swelling degree, each sample was soaked in water for 30 minutes and then it was carefully placed on the weight scale. A small amount of water was added to rectify any loss during sample collection and transport, any excess of water was removed by absorbent paper. The calculation of water adsorption kinetic was estimated by placing each sample in contact with a slight excess of water for the selected time, therefore the excess of not absorbed water was quickly removed by absorbent paper. The wet sample was weighted and the value of water absorbed at time *t* was normalized with respect to the value of the water absorbed after 30 min. For the determination of swelling-deswelling cycles performances, after the first determination of equilibrium swelling, all the wet samples were placed between two sheets of absorbent paper and squeezed with a 50 g weight for about 5 min. The squeezed samples were weighted, then immersed again in water and prepared for a new swelling degree determination. This operation sequence was repeated 5 times.

The porosity of the dried samples was calculated as percentage by measuring the adsorbed volume of cyclohexane versus the total volume of each sample. The porosity of the cryo-gel samples was measured according to Archimedes' principle using an adapted gravity bottle and determined by the following equation,

$$Porosity\ \% = \frac{V_{pores}}{V_{sample}} \times 100 = \frac{m_w - m_d}{m_1 - m_2 + m_w} \times 100 \qquad (11)$$

where m_d is the mass of the dried cryogel, m_w is the mass of the cyclohexane-saturated cryogel, m_1 is the mass of the gravity bottle filled with cyclohexane, m_2 is the mass of the gravity bottle containing cyclohexane and cryogel. To remove residual gas into the cryogels, the samples were immersed in cyclohexane under reduced pressure before their transfer inside the gravity bottle.

Compression tests of wet pHEMA-based cryogels were performed using a Thermo Scientific RS6000 rotational rheometer in uniaxial compression mode. Equilibrium swollen cryogel samples were cut in pieces of 6 mm height, and placed in between the rheometer plates (20 mm diameter) at 25 °C. The rheometer gap were reduced until the sample was firmly kept between the plates, then a pre-strain of 0.4 mm was imposed. The samples was then compressed up to 50% of the initial height with a speed of 15 mm/min.

The adsorption properties of all the samples were examined through the adsorption of MB dye in aqueous solution. In a typical experiment, ~ 5 mg of sponges were added in 2 mL of MB solution with a starting concentration of 1.5×10^{-5} M (4.8 mg/L), at room temperature and with a neutral pH. The adsorption tests were run in parallel for each sample. Every 30 minutes, the solutions were collected, and the adsorption of MB onto materials was evaluated measuring the variation of the dye absorbance at 664 nm. The dye adsorption on the vial walls was also checked, as a reference, in the absence of the adsorbent materials.

With the aim of regenerating the sponges, they were immersed in de-ionized water and irradiated by an UV lamp, centered at 368 nm, with an irradiance of 4 mW/cm^2, for a total time of 5 hrs.

FTIR characterization was performed by a Perkin-Elmer Spectrum 1000 spectrometer. The analyzed samples, in the form of tablet, were obtained by mixing ~1 mg of milled sponge with 300 mg of KBr powders in an agate mortar and pressing with a press. In order to evaluate the adsorption and the eventual photodegradation of the adsorbed dye under UV light irradiation, after the absorption process and after the UV light irradiation a portion of each sample was dried, at 100 °C overnight and analyzed by FTIR spectroscopy, as reported before.

Conclusion

We have presented the formulation of innovative nanocomposites based on pHEMA polymeric cryogel containing GO and ZnO nanostructures. The formulated materials displayed a noteworthy adsorption aptitude versus MB dye. Particularly, sponges enriched with ZnO by ALD have acquired photocatalytic properties, allowing recyclability after their irradiation by UV light. The amount of adsorbed MB at equilibrium of 0.73, 0.97, 0.82, and 0.94 mg per g of materials, for pHEMA, pHEMA-GO, ZnO/pHEMA, and ZnO/pHEMA-GO, respectively, clearly indicate as GO plays an important role during adsorption. Nevertheless, while pHEMA and pHEMA-GO lose their adsorption capability after several cycles, the samples coated with ZnO are able to preserve it, thanks to the regeneration via UV light irradiation. The recyclability and mechanical tests revealed as ZnO/pHEMA materials can be easily-reused, explicating an effective remediation action versus organic pollutants. These results can open a new route in the formulation of materials for wastewater treatment and purification. Furthermore, the adsorption process can be modulated and/or addressed to different emerging pollutants (drugs and pesticides), by changing the polymer nature, architecture and/or composite formulation.

Acknowledgements

We wish to thank Giuseppe Pantè (CNR-IMM) for technical assistance.

Authors contribution: S. C. Carroccio and M. Ussia conceived the project idea and provided TGA measurements; T. Mecca, M. Ussia and F. Cunsolo synthesized the cryo-sponges and performed the swelling-deswelling and porosity determinations; A. Di Mauro and G. Impellizzeri supervised the ALD syntheses and provided kinetic calculations; M. Ussia and A. Di Mauro performed adsorption and photocatalytic tests; A. Di Mauro achieved FT-IR and XRD characterizations; A. Di Mauro, G. Impellizzeri, and S. C. Carroccio wrote the paper; G. Nicotra, and C. Spinella, performed the TEM analyses; P. Cerruti achieved the mechanical tests; V. Privitera reviewed and commented the manuscript at all stages.

References

[1] Shannon, M. A.; Bohn, P. W.; Elimelech, M.; Georgiadis, J. G.; Marĩas, B. J.; Mayes, A. M. Science and Technology for Water Purification in the Coming Decades. *Nature* **2008**, 452, 301–310.

[2] Gaya, U. I.; Abdullah, A. H. Heterogeneous Photocatalytic Degradation of Organic Contaminants over Titanium Dioxide: A Review of Fundamentals, Progress and Problems. *J. Photochem. Photobiol. C Photochem. Rev*. **2008**, 9, 1–12.

[3] Liu, F.; Chung, S.; Gahee, O.; Seo, T. S. Three-dimensional Graphene Oxide Nanostructure for Fast and Efficient Water-soluble Dye Removal. *ACS Appl. Mater. Interfaces.* **2012**, 4, 922–927.

[4] Gupta, V.K.; Saleh, T.A. Sorption of Pollutants by Porous Carbon, Carbon Nanotubes and Fullerene- an Overview. *Environ. Sci. Pollut. Res.* **2013**, 20, 2828–2843.

[5] Ganigar, R.; Rytwo, G.; Gonen, Y.; Radiana, A.; Mishael, Y. G. Polymer–clay Nanocomposites for the Removal of Trichlorophenol and Trinitrophenol from Water. *Appl. Clay Sci.* **2010**, 49, 311–316.

[6] Srinivasan, R. Advances in Application of Natural Clay and Its Composites in Removal of Biological, Organic, and Inorganic Contaminants from Drinking Water. *Adv. Mater. Sci. Eng.* **2011**, 2011, 1–17.

[7] Salzano de Luna, M.; Castaldo, R.; Altobelli, R.; Gioiella, L.; Filippone, G.; Gentile, G.; Ambrogi, V. Chitosan Hydrogels Embedding Hyper-crosslinked Polymer Particles as Reusable Broad-spectrum Adsorbents for Dye Removal. *Carbohydr. Polym.* **2017**, 177, 347–354.

[8] Vakili, M.; Rafatullah, M.; Salamatinia, B.; Abdullah, A. Z.; Ibrahim, M. H.; Tan, K. B.; Gholami, Z.; Amouzgar, P. Application of Chitosan and Its Derivatives as Adsorbents for Dye Removal from Water and Wastewater: a Review. *Carbohydr. Polym*. **2014**, 113, 115–130.

[9] Chang, C.; Zhang, L. Cellulose-based Hydrogels: Present Status and Application Prospects. *Carbohydr. Polym*. **2011**, 84, 40–53.

[10] Dutta, K.; De, S. Smart Responsive Materials for Water Purification: an Overview. *J. Mater. Chem. A* **2017**, 5, 22095-22112.

[11] Loo, S. L.; Krantz, W. B.; Fane, A. G.; Gao, Y.; Lim, T. T.; Hu, X. Bactericidal Mechanisms Revealed for Rapid Water Disinfection by Superabsorbent Cryogels Decorated with Silver Nanoparticles. *Environ. Sci. Technol.* **2015**, 49, 2310–2318.

[12] Wang, D. C.; Yu, H. Y.; Song, M. L.; Yang, R. T.; Yao, J. M. Superfast Adsorption–Disinfection Cryogels Decorated with Cellulose Nanocrystal/Zinc Oxide Nanorod Clusters for Water-Purifying Microdevices *ACS Sustain. Chem. Eng.* **2017**, 5, 6776–6785.

[13] Chong, M. N.; Jin, B.; Chow, C. W. K.; Saint C. Recent Developments in Photocatalytic Water Treatment Technology: A Review *Water Res.*, **2010**, 44, 2997–3027.

[14] Marin, M. L.; Santos-Juanes, L.; Arques, A.; Amat, A. M.; Miranda, M. A. Organic Photocatalysts for the Oxidation of Pollutants and Model Compounds. *Chem. Rev.* **2012**, 112, 1710–1750.

[15] Kanakaraju, D.; Glass, B. D.; Oelgem, M. Advanced Oxidation Process-mediated Removal of Pharmaceuticals from Water: A Review. *J Environ Manage.* **2018**, 219, 189-207.

[16] Di Mauro, A.; Fragalà, M. E.; Privitera, V.; Impellizzeri, G. ZnO for Application in Photocatalysis: from Thin Films to Nanostructures *Mater. Sci. Semicond. Process.* **2017**, 69, 44–51.

[17] Scuderi, V.; Impellizzeri, G.; Romano, L.; Scuderi, M.; Brundo, M. V.; Bergum, K.; Zimbone, M.; Sanz, R.; Buccheri, M. A.; Simone, F.; Nicotra, G.; Svensson, B. G.; Grimaldi, M. G.; Privitera, V. An Enhanced Photocatalytic Response of Nanometric TiO_2 Wrapping of Au Nanoparticles for Eco-friendly Water Applications. *Nanoscale* **2014**, 6, 11189–11195.

[18] Scuderi, V.; Impellizzeri, G.; Zimbone, M.; Sanz, R.; Di Mauro, A.; Buccheri, M. A.; Miritello, M.; Terrasi, A.; Rappazzo, G.; Nicotra, G.; Privitera, V. Rapid Synthesis of Photoactive Hydrogenated TiO_2 Nanoplumes *Appl. Catal. B Environ.* **2016**, 183, 328–334.

[19] Di Mauro, A.; Cantarella, M.; Nicotra, G.; Privitera, V.; Impellizzeri, G. Low Temperature Atomic Layer Deposition of ZnO: Applications in Photocatalysis. *Appl. Catal. B Environ.* **2016**, 196, 68–76.

[20] Pelaez, M.; Nolan, N. T.; Pillai, S. C.; Seery, M. K.; Falaras, P.; Kontos, A. G.; Dunlop, P. S. M.; Hamilton, J. W. J.; Byrne, J. A.; O'Shea, K.; Entezari, M. H.; Dionysiou, D. D. A Review on the Visible Light Active Titanium Dioxide Photocatalysts for Environmental Applications *Appl. Catal. B Environ.* **2012**, 125, 331–349.

[21] Lee, K. M.; Lai, C. W.; Ngai, K. S.; Juan, J. C. Recent Developments of Zinc Oxide Based Photocatalyst in Water Treatment Technology: a Review. *Water Research* **2016**, 88, 428-448.

[22] Babaheydaria, A. K.; Salavati-Niasarib, M.; Khansaric, A. Solvent-less Synthesis of Zinc Oxide Nanostructures from Zn (Salen) as Precursor and their Optical Properties. *Particuology* **2012**, 10, 759–764.

[23] Salavati-Niasari, M.; Davar, F.; Mazaheri, M. Preparation of ZnO Nanoparticles from [bis (acetylacetonato) Zinc (II)]–oleylamine Complex by Thermal Decomposition. *Materials Letters* **2008**, 62, 1890–1892.

[24] Mir, N.; Salavati-Niasari, M.; Davarc, F. Preparation of ZnO Nanoflowers and Zn Glycerolate Nanoplates Using Inorganic Precursors via a Convenient Rout and Application in Dye Sensitized Solar cells. *Chemical Engineering Journal* **2012**, 181– 182, 779– 789.

[25] Monsef, R.; Ghiyasiyan-Arani, M.; Salavati-Niasaria, M. Application of Ultrasound-aided Method for the Synthesis of NdVO4 Nano-photocatalyst and Investigation of Eliminate Dye in Contaminant Water *Ultrasonics – Sonochemistry* **2018**, 42, 201–211.

[26] Salavati-Niasari, M.; Mir, N.; Davar, F. Nanosphericals and Nanobundles of ZnO: Synthesis and Characterization *Journal of Alloys and Compounds* **2011**, 509, 61–65.

[27] Ussia, M.; Bruno, E.; Spina, E.; Vitalini, D.; Pellegrino, G.; Ruffino, F.; Privitera, V.; Carroccio, S. C. Freestanding Photocatalytic Materials Based on 3D Graphene and Polyporphyrins. *Sci. Rep.* **2018**, 8, 1–12.

[28] Ghanbari, D.; Salavati-Niasari, M.; Ghasemi-Kooch, M. A Sonochemical Method for Synthesis of Fe_3O_4 Nanoparticles and Thermal Stable PVA-based Magnetic Nanocomposite. *Journal of Industrial and Engineering Chemistry* **2014**, 20, 3970–3974.

[29] Chen, Y.; Li, A.; Huang, Z.-H.; Wang, L.-N.; Kang, F. Porphyrin-based Nanostructures for Photocatalytic Applications. *Nanomaterials*, 2016, **6**, 51.

[30] Chen, X.; Mao, S. S. Titanium Dioxide Nanomaterials: Synthesis, Properties, Modifications, and Applications. *Chem. Rev.* **2007**, 107, 2891–2959.

[31] Li, Q.; Mahendra, S.; Lyon, D. Y.; Brunet, L.; Liga, M. V.; Li, D.; Alvarez, P. J. J. Antimicrobial Nanomaterials for Water Disinfection and Microbial Control: Potential Applications and Implications. *Water Res.* **2008**, 42, 4591–4602.

[32] Srikanth, B.; Goutham, R.; Badri, N. R.; Ramprasath, A.; Gopinath, K. P.; Sankaranarayanan, A. R. Recent Advancements in Supporting Materials for Immobilised Photocatalytic Applications in Waste Water Treatment. *J. Environ. Manage*. **2017**, 200, 60–78.

[33] Cantarella, M.; Sanz, R.; Buccheri, M. A.; Ruffino, F.; Rappazzo, G.; Scalese, S.; Impellizzeri, G.; Romano, L.; Privitera, V. Immobilization of Nanomaterials in PMMA Composites for Photocatalytic Removal of Dyes, Phenols and Bacteria from Water. *J. Photochem. Photobiol. A Chem.* **2016**, 321, 1–11.

[34] Perreault, F.; De Faria, A. F.; Elimelech M. Environmental Applications of Graphene-based Nanomaterials. M. *Chem. Soc. Rev.* **2015**, 44, 5861–5896.

[35] Kemp, K. C.; Seema, H.; Saleh, M.; Le, N. H.; Mahesh, K.; Chandra, V.; Kim, K. S. Environmental Applications Using Graphene Composites: Water Remediation and Gas Adsorption. *Nanoscale* **2013**, 5, 3149.

[36] Filice, S.; D'Angelo, D.; Libertino, S.; Nicotera, I.; Kosma, V.; Privitera, V.; Scalese, S. Graphene Oxide and Titania Hybrid Nafion Membranes for Efficient Removal of Methyl Orange Dye from Water. *Carbon* **2015**, 82, 489-499.

[37] Yang, S. T.; Chen, S.; Chang, Y.; Cao, A.; Liu, Y.; Wang H. Removal of Methylene Blue from Aqueous Solution by Graphene Oxide. *J. Colloid Interface Sci.* **2011**, 359, 24–29.

[38] Ramesha, G. K.; Kumara, A. V.; Muralidhara, H. B; Sampath, S. Graphene and Graphene Oxide as Effective Adsorbents Toward Anionic and Cationic Dyes. *J. Colloid Interface Sci.* **2011**, 361, 270–277.

[39] Kuilla, T.; Bhadra, S.; Yao, D.; Kim, N. H.; Bose, S.; Lee J.H. Recent Advances in Graphene Based Polymer Composites. *Progress in Polymer Science* **2010**, 35**,** 1350-1375.

[40] Potts, J. R.; Dreyer, D. R.; Bielawski, C. W.; Ruoff, R. S. Graphene-based Polymer Nanocomposites. *Polymer* **2011**, **52**, 5–25.

[41] Periasamy, A. P.; Wu, W. P.; Ravindranath, R.; Roy, P.; Lin, G. L.; Chang, H. T. Polymer/reduced Graphene Oxide Functionalized Sponges as Superabsorbents for Oil Removal and Recovery. *Mar. Pollut. Bull.* **2017**, 114, 888–895.

[42] Huang, Y.; Zeng, M.; Ren, J.; Wang, J.; Fan, L.; Xu, Q. Preparation and Swelling Properties of Graphene Oxide/poly(acrylic acid-co-acrylamide) Super-absorbent Hydrogel Nanocomposites. *Colloids Surfaces A Physicochem. Eng. Asp.* **2012**, 401, 97–106.

[43] Sha, J.; Gao, Y.; Wu, T.; Chen, X.; Cordie, T.; Zhao, H.; Xie, L.; Ma, Y.; Turng, L. Biocompatible Graphene Nanosheets Grafted with Poly(2-hydroxyethyl methacrylate) Brushes via Surface-initiated. ARGET ATRP. *RSC Adv.* **2016**, 6, 35641–35647.

[44] Okay, O. (ed.), Polymeric Cryogels, Advances in Polymer Science 263, Springer, **2014**.

[45] Kumar, A. (ed.), Supermacroporous Cryogels: Biomedical and Biotechnolgic applications, CRC Press – Taylor & Francis Group, **2016**.

[46] Di Mauro, A.; Cantarella, M.; Nicotra, G.; Pellegrino, G.; Gulino, A.; Brundo, M. V.; Privitera, V.; Impellizzeri, G. Novel Synthesis of ZnO/PMMA Nanocomposites for Photocatalytic Applications. *Sci. Rep.* **2017**, 7, 1–12.

[47] Pellegrino, G.; Carroccio, S. C.; Ruffino, F.; Condorelli, G. G.; Nicotra, G.; Privitera, V.; Impellizzeri, G. Polymeric Platform for the Growth of Chemically Anchored ZnO Nanostructures by ALD. *RSC Adv.* **2018**, 8, 521–530.

[48] Cai, R.; Wu, J. G.; Sun, L.; Liu, Y. J.; Fang, T.; Zhu, S.; Li, S. Y.; Wang, Y.; Guo, L. F.; Zhao, C. E.; Wei, A. 3D Graphene/ZnO Composite with Enhanced Photocatalytic Activity. *Mater. Des.* **2016**, 90, 839–844.

[49] Singh, S.; Mahalingam, H.; Singh, P. K. Polymer-supported Titanium Dioxide Photocatalysts for Environmental Remediation: A Review. *Appl. Catal. A Gen.* **2013**, 462–463, 178–195.

[50] Di Mauro, A.; Fragalà, M. E.; Privitera, V.; Impellizzeri, G. ZnO for Application in Photocatalysis: from Thin Films to Nanostructures. *Mater. Sci. Semicond. Process.* **2017**, 69, 44–51.

[51] Saleem, M.; Fang, L.; Ruan, H.B.; Wu, F.; Huang, Q.L.; Xu, C.L.; Kong, C.Y. Effect of Zinc Acetate Concentration on the Structural and Optical Properties of ZnO Thin Films Deposited by Sol-Gel Method *Intl. J. Phy. Sci.* **2012**, 7(23), 2971–2979.

[52] Japić, D.; Marinšek, M.; Crnjak, O. Z. Effect of ZnO on the Thermal Degradation Behaviour of Poly(methyl methacrylate) Nanocomposites. *Acta Chim. Slov*. **2016,** 3, 535–543.

[53] Yu, M.; Wang, A.; Wang, Y.; Li, C.; Shi, G. An Alumina Stabilized ZnO–Graphene Anode for Lithium Ion Batteries via Atomic Layer Deposition *Nanoscale*, 2014, **6**, 11419–11424.

[54] Azizi, S.; Ahmad, M.; Mahdavi, M.; Abdolmohammadi, S. Preparation, Characterization, and Antimicrobial Activities of ZnO Nanoparticles/Cellulose Nanocrystal Nanocomposites. *BioResources* **2013**, 8, 1841–1851.

[55] Loo, S. L.; Krantz, W. B.; Fane, A. G.; Hu, X.; Lim, T. T. Effect of Synthesis Routes on the Properties and Bactericidal Activity of Cryogels Incorporated with Silver Nanoparticles. *RSC Adv*. **2015**, 5, 44626–44635.

[56] Loo, S. L.; Fane, A. G.; Lim, T. T.; Krantz, W. B.; Liang, Y. N.; Liu, X.; Hu, X. Superabsorbent Cryogels Decorated with Silver Nanoparticles as a Novel Water Technology for Point-of-use Disinfection. *Environmental Science & Technology* **2013**, 47 (16), 9363-9371.

[57] Liu, C.; Liu, X.; Quan, C.; Li, X.; Chen, C.; Kang, H.; Hu, W.; Jiang, Q.; Zhang, C. Poly(γ-glutamic acid) Induced Homogeneous Mineralization of the Poly(ethylene glycol)-co-2-hydroxyethyl Methacrylate Cryogel for Potential Application in Bone Tissue Engineering. *RSC Adv.* **2015**,5,20227

[58] Zhai, M.; Ma, F.; Li, J.; Wan, B.; Yu, N. Preparation and Properties of Cryogel Based on Poly (hydroxypropyl methacrylate) J., *Biomater. Sci. Polym. Ed.* **2018**, 29, 1401-1425.

[59] Kumari, J.; Kumar, A. Development of Polymer Based Cryogel Matrix for Transportation and Storage of Mammalian Cells. *Sci. Rep.* **2017**, 7, 41551.

[60] Petriciolet, A. B.; Mendoza-Castillo, D. I.; Reynel-Ávila, H. E. *Adsorption Processes for Water Treatment and Purification*, Springer 2017

[61] Qiu, H.; Pan, L.L.; Zhang, Q.; Zhang, W.; Zhang, Q. Critical Review in Adsorption Kinetic Models *J Zhejiang .Univ Sci A* **2009**, 10**,** 716–724.

[62] Largitte, L.; Pasquier, R. A Review of the Kinetics Adsorption Models and Their Application to the Adsorption of Lead by an Activated carbon. *Chem. Eng. Res. Des.* **2016**, 109, 495–504.

[63] Lagergren, S.; *Kungliga Svenska Vetenskapsakademiens Handlingar*, **1898** 24 (4), 1-39.

[64] Ho, Y. S. Review of Second-order Models for Adsorption Systems. *J. Hazard. Mater.* **2006**, 136, 681–689.

[65] Aydin, Y. A.; Aksoy, N. D. Adsorption of Chromium on Chitosan: Optimization, Kinetics and Thermodynamics *Chem. Eng. J.* **2009**, 151, 188–194.

[66] Ho, Y. S.; McKay, G. Kinetic Models for the Sorption of Dye from Aqueous Solution by Wood. *Process Saf. Environ. Prot.* **1998**, 76, 183–191.

[67] Ho, Y. S.; McKay, G. A Comparison of Chemisorption Kinetic Models Applied to Pollutant Removal on Various Sorbents. *Process Saf. Environ. Prot.* **1998**, 76, 332–340.

[68] Sahiner, N.; Demirci, S. The Use of Graphene Oxide-embedded Superporous poly(2-hydroxyethylmethacrylate) Cryogels for p-(aniline) Conductive Polymer Synthesis and their use in Sensor Applications. *Materials and Design* **2017**, 120, 47–55.

[69] Kumpan, N.; Poonsawat, T.; Chaicharoenwimolkul, L.; Pornsuwan, S.; Somsook, E. Ferrocenated Nanocatalysts Derived from the Decomposition of Ferrocenium in Basic Solution and their Aerobic Activities for the Rapid Decolorization of Methylene Blue and the Facile Oxidation of Phenylboronic acid. *RSC Adv.* **2017**, 7, 5759–5763.

[70] Avcibasi, N.; Uygun, M.; Corman, M.E.; Akgol, S.; Denizli, A. Application of Supermacroporous Monolithic Hydrophobic Cryogel in Capturing of Albumin. *Appl Biochem Biotechnol* **2010**, 162, 2232-2243.

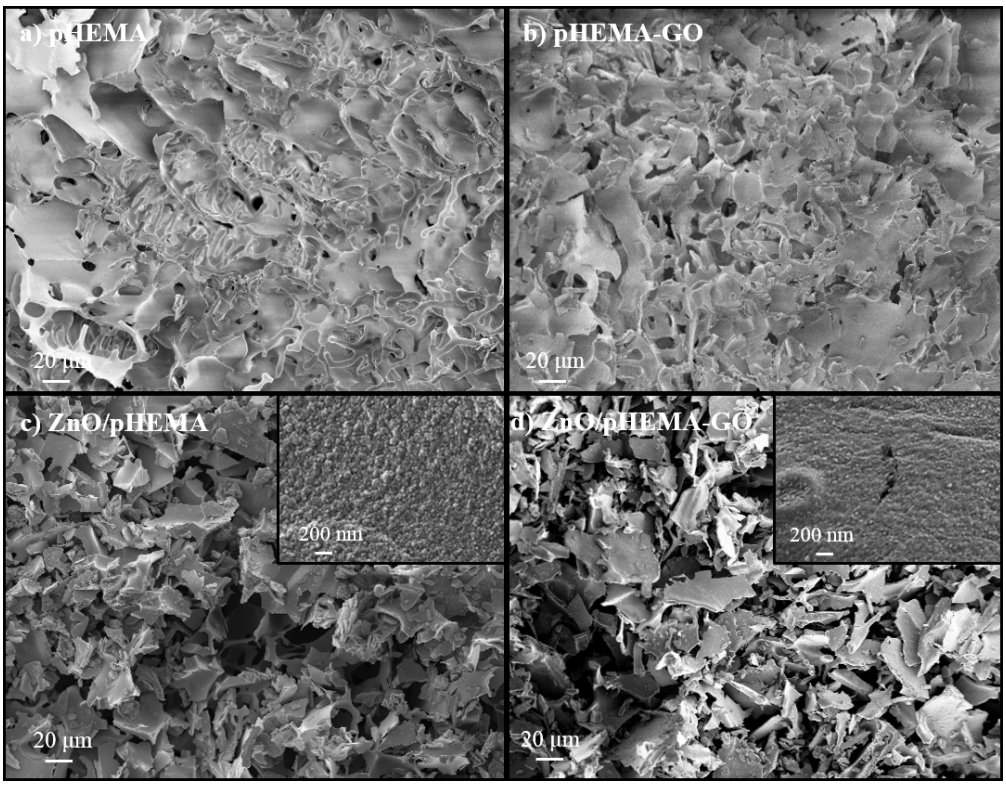

Figure 1. SEM images of pHEMA (a), pHEMA-GO (b), ZnO/pHEMA (c), and ZnO/pHEMA-GO (d), together with high magnification images reported as insets of figures (c) and (d).

182x141mm (150 x 150 DPI)

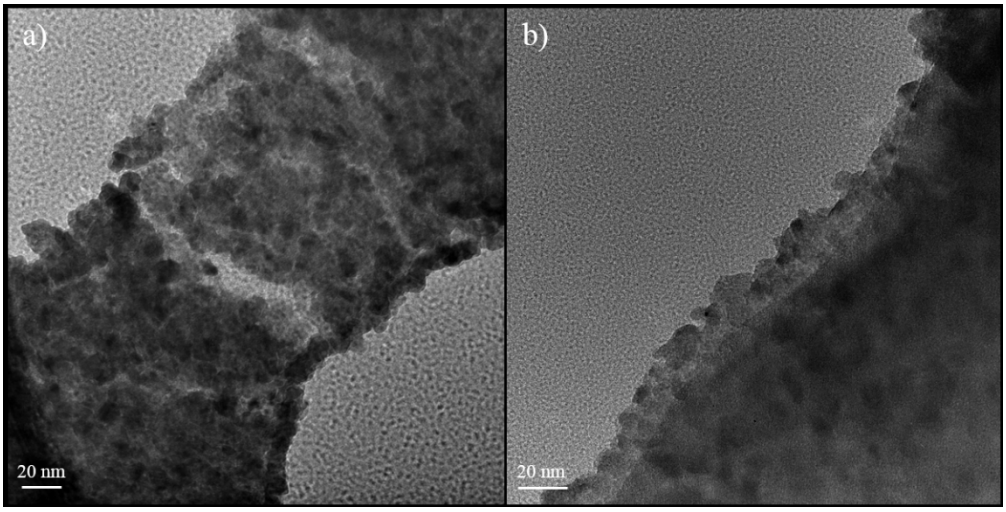

Figure 2. TEM images of plan view (a) and cross section (b).

201x101mm (150 x 150 DPI)

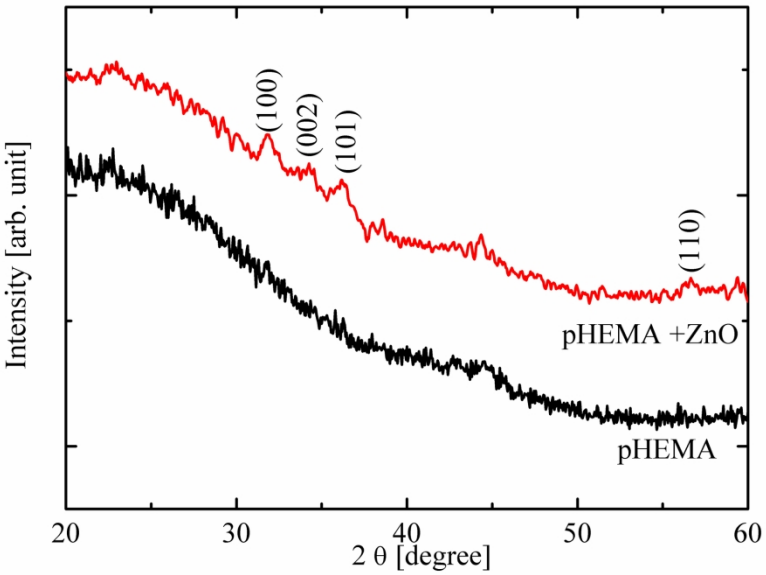

Figure 3. XRD patterns of pHEMA, and ZnO/pHEMA (from the bottom to the top).

201x140mm (300 x 300 DPI)

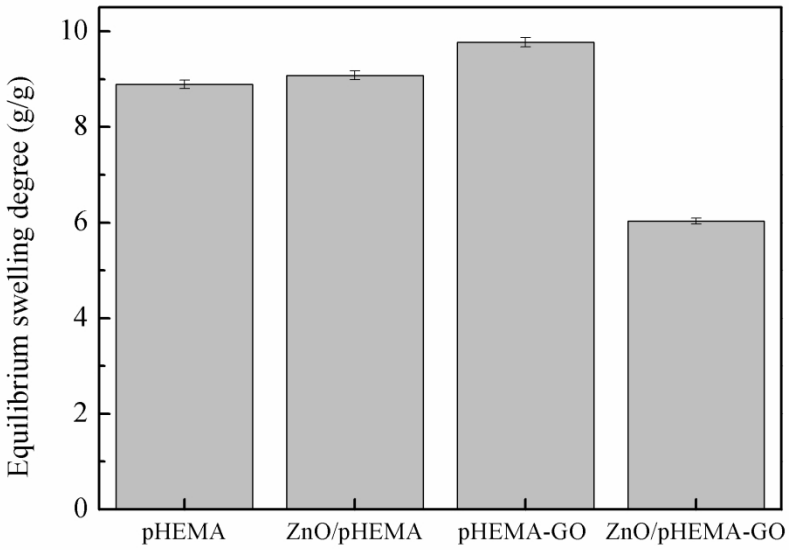

Figure 4. Equilibrium swelling degree of pHEMA, ZnO/pHEMA, pHEMA-GO, and ZnO/pHEMA-GO.

201x140mm (300 x 300 DPI)

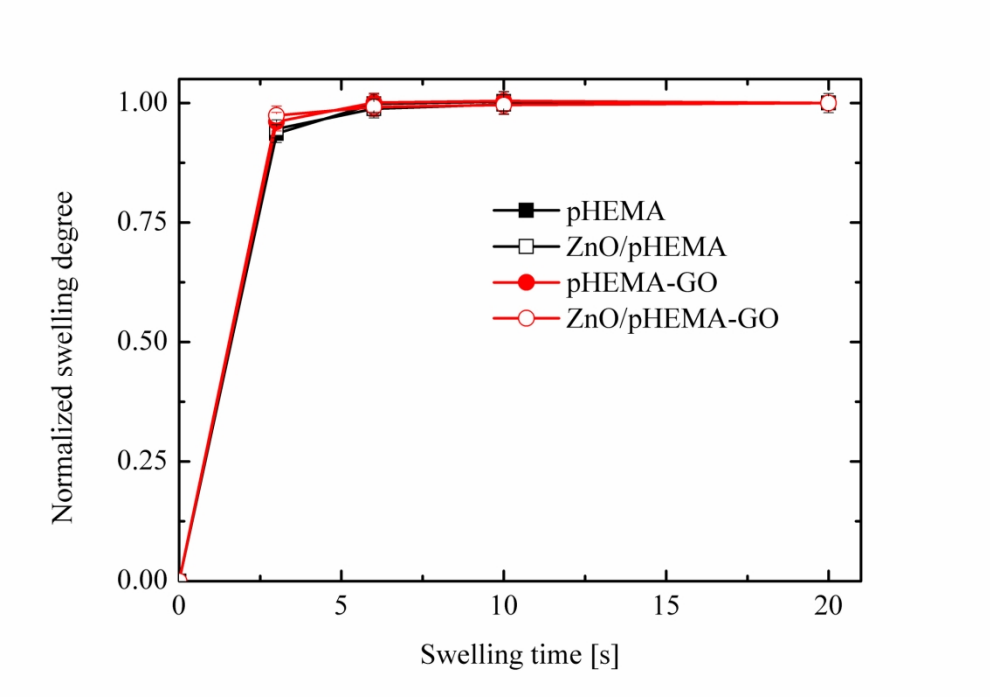

Figure 5. Dynamic swelling profiles of pHEMA, ZnO/pHEMA, pHEMA-GO, and ZnO/pHEMA-GO.

201x140mm (300 x 300 DPI)

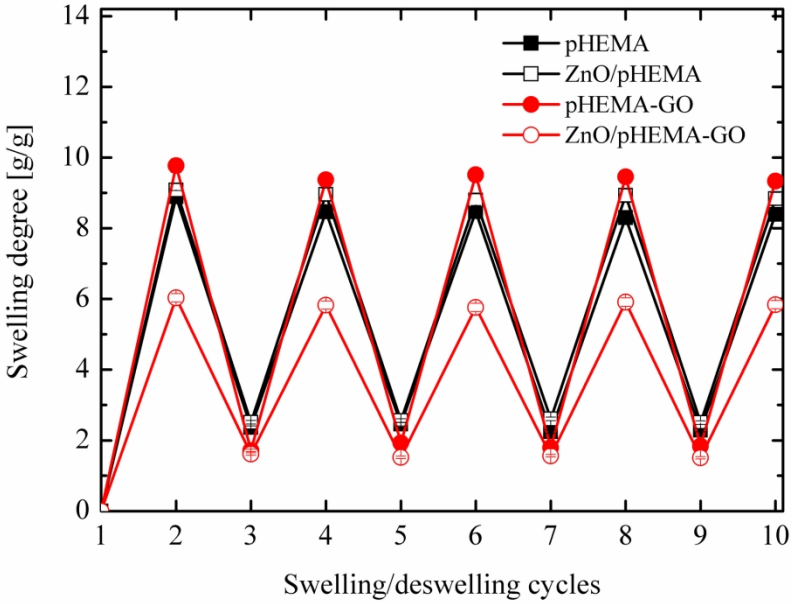

Figure 6. Swelling/ deswelling degree cycles of all pHEMA samples

201x140mm (300 x 300 DPI)

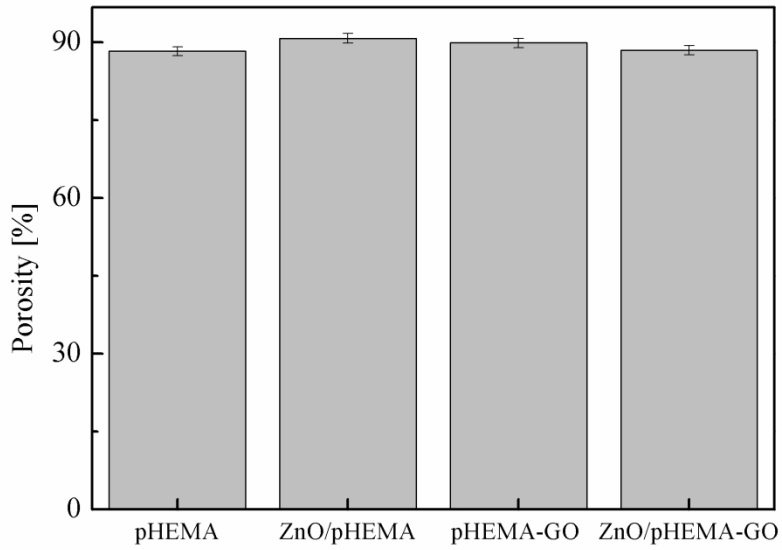

Figure 7. Porosity of pHEMA, ZnO/pHEMA, pHEMA-GO, and ZnO/pHEMA-GO cryogels.

201x140mm (300 x 300 DPI)

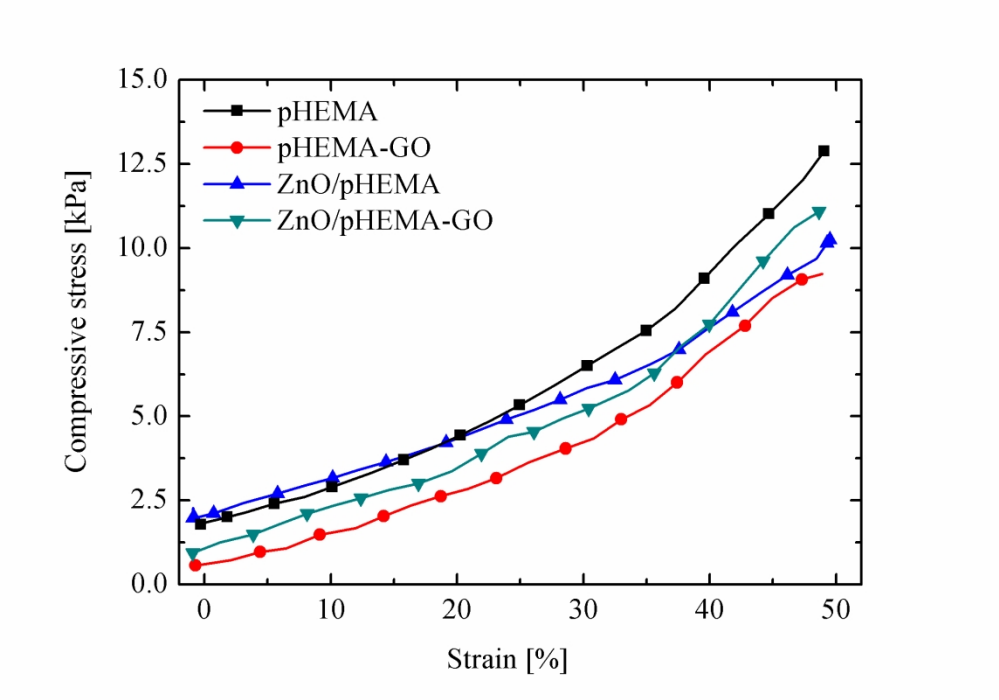

Figure 8. Stress-strain curves of pHEMA, ZnO/pHEMA, pHEMA-GO, and ZnO/pHEMA-GO wet cryogels subjected to compression test.

201x141mm (300 x 300 DPI)

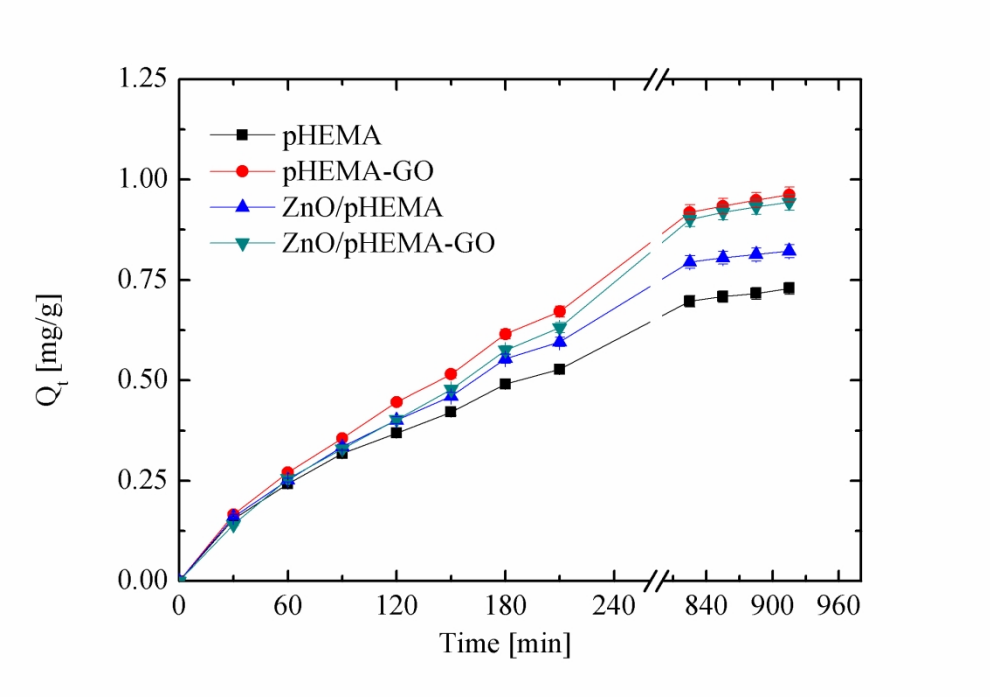

Figure 9. MB adsorption capacity versus time for pHEMA, pHEMA-GO, ZnO/pHEMA, and ZnO/pHEMA-GO.

201x140mm (300 x 300 DPI)

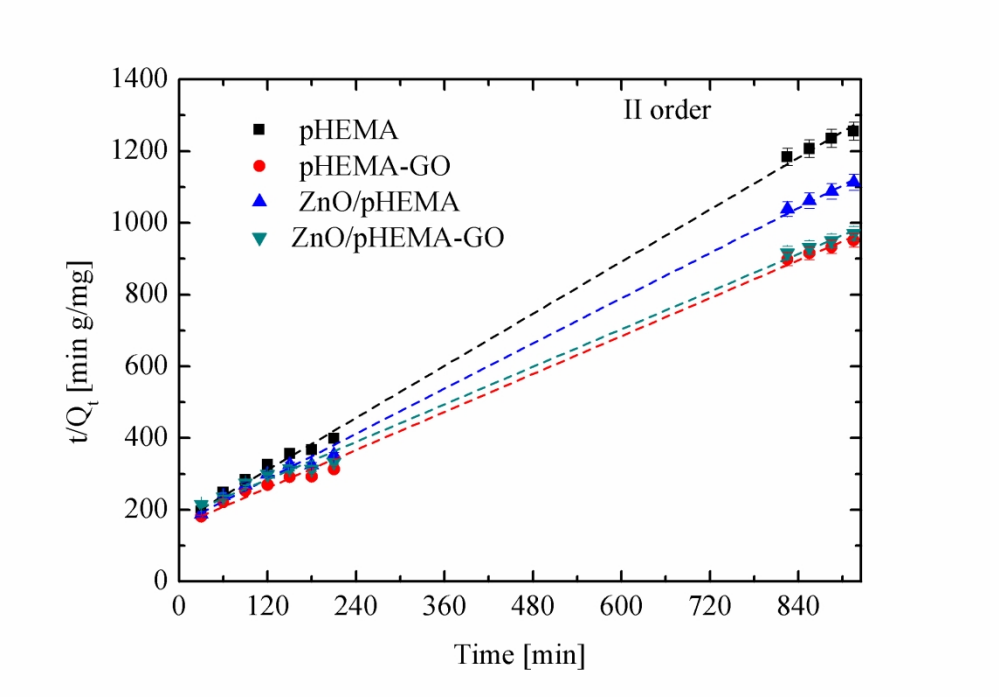

Figure 10. Adsorption kinetic of MB for pHEMA (squares), pHEMA-GO (circles), ZnO/pHEMA (up triangles), and ZnO/pHEMA-GO (down triangles) fitted with the pseudo-second-order model (dashed lines).

201x140mm (300 x 300 DPI)

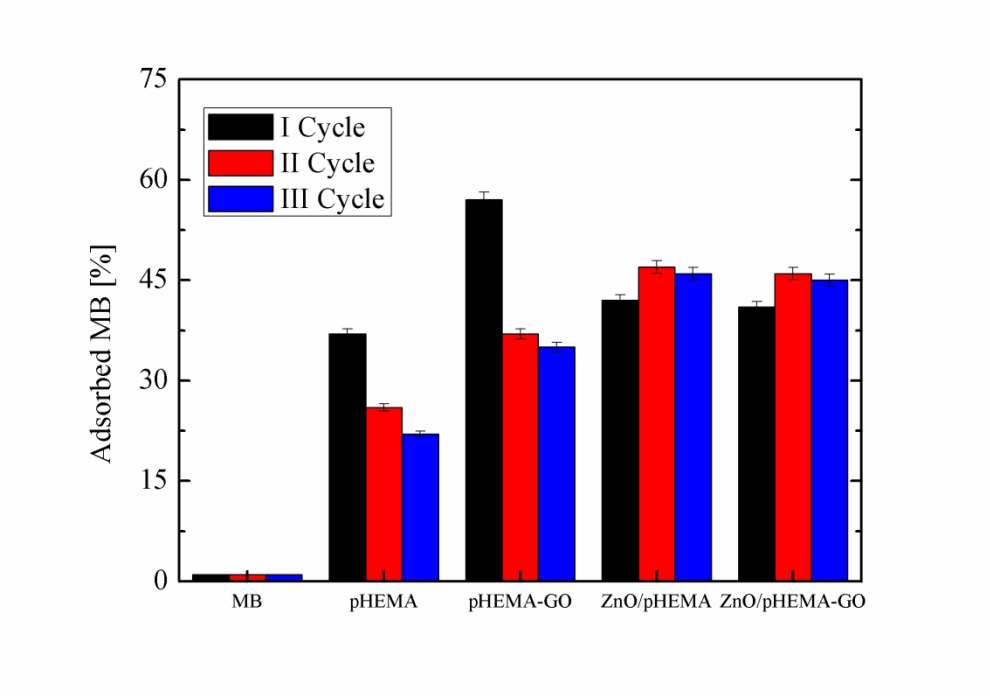

Figure 11. Recyclability after three adsorption cycles of MB, pHEMA, pHEMA GO, ZnO/pHEMA and ZnO/pHEMA-GO.

201x140mm (300 x 300 DPI)

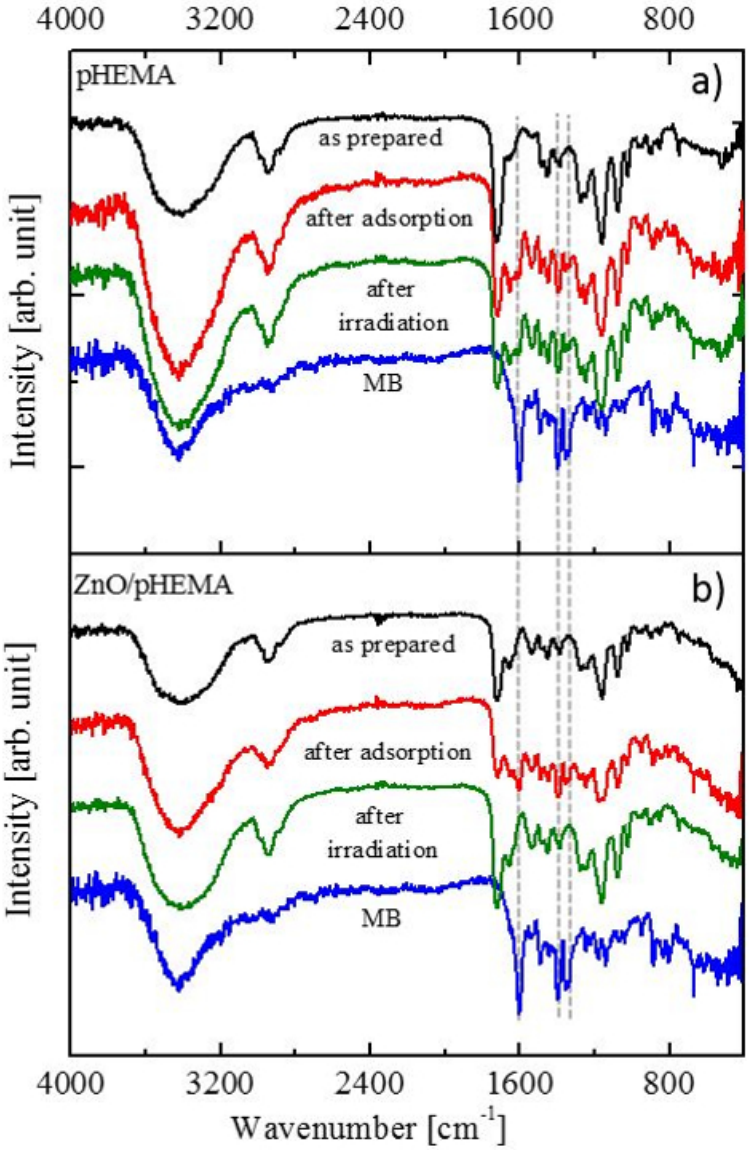

Figure 12. FTIR spectra measured on pHEMA (a), and on ZnO/pHEMA (b), as prepared (first spectrum from the top), after MB adsorption (second spectrum from the top), and after regeneration by UV light irradiation. The spectrum of pure MB is shown as reference. The spectra were vertically shifted for clarity. Vertical dashed lines indicate the typical stretching peaks of MB.

124x190mm (100 x 100 DPI)

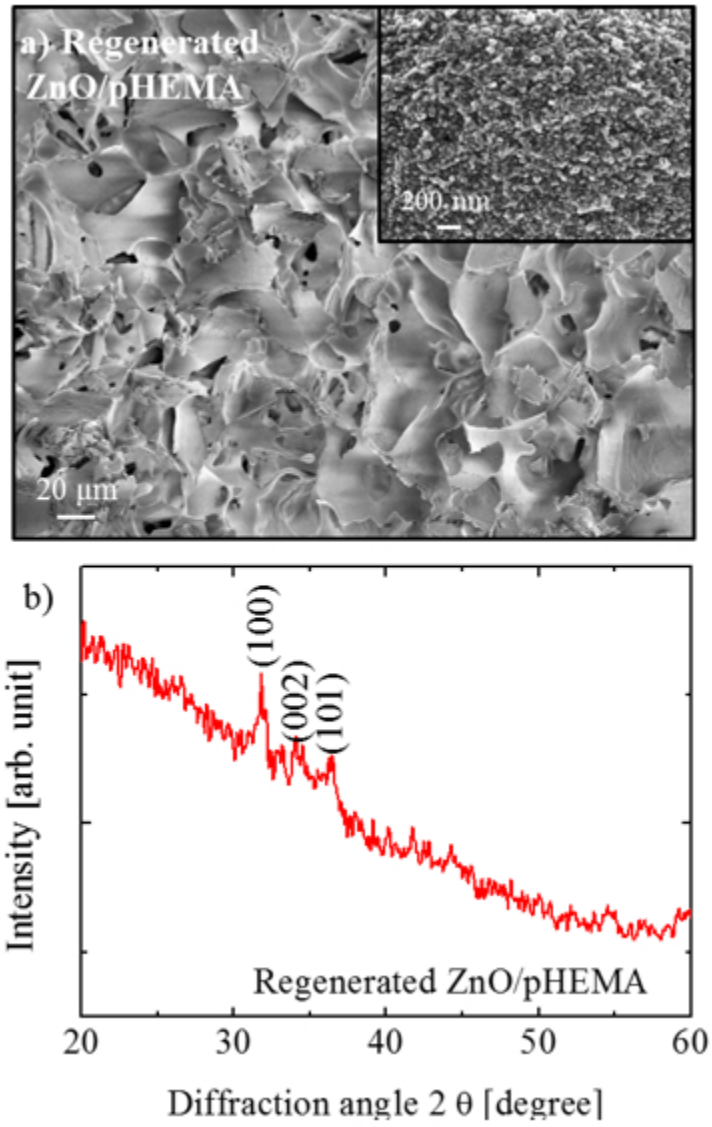

Figure 13. a) SEM analysis of ZnO/pHEMAafter the regeneration, and high magnification (inset); b) XRD diffractogram of the regenerated ZnO/pHEMA.

102x152mm (96 x 96 DPI)

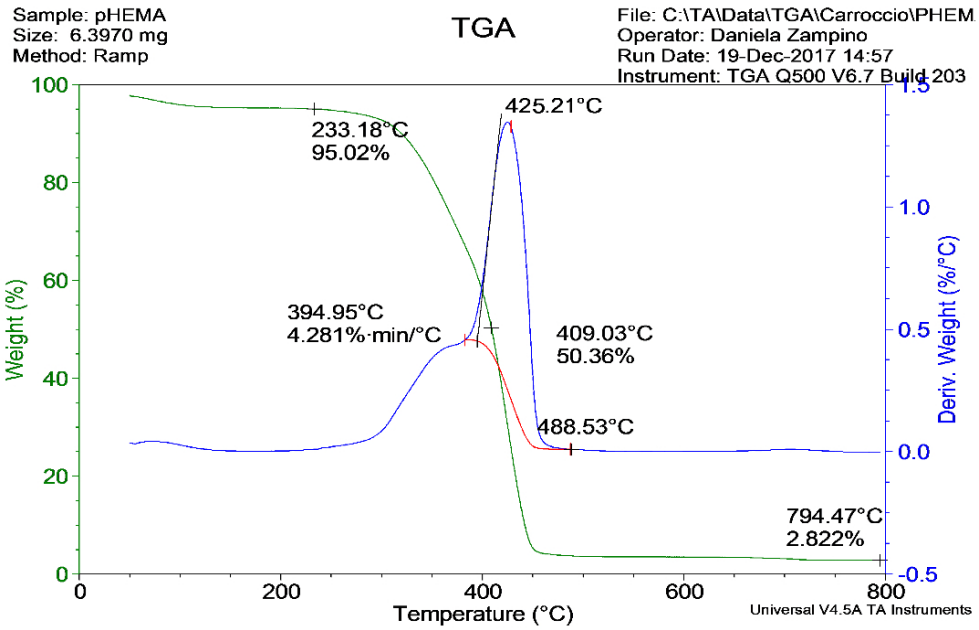

Figure S1. TG and DTG profiles of PHEMA sample.

126x83mm (220 x 220 DPI)

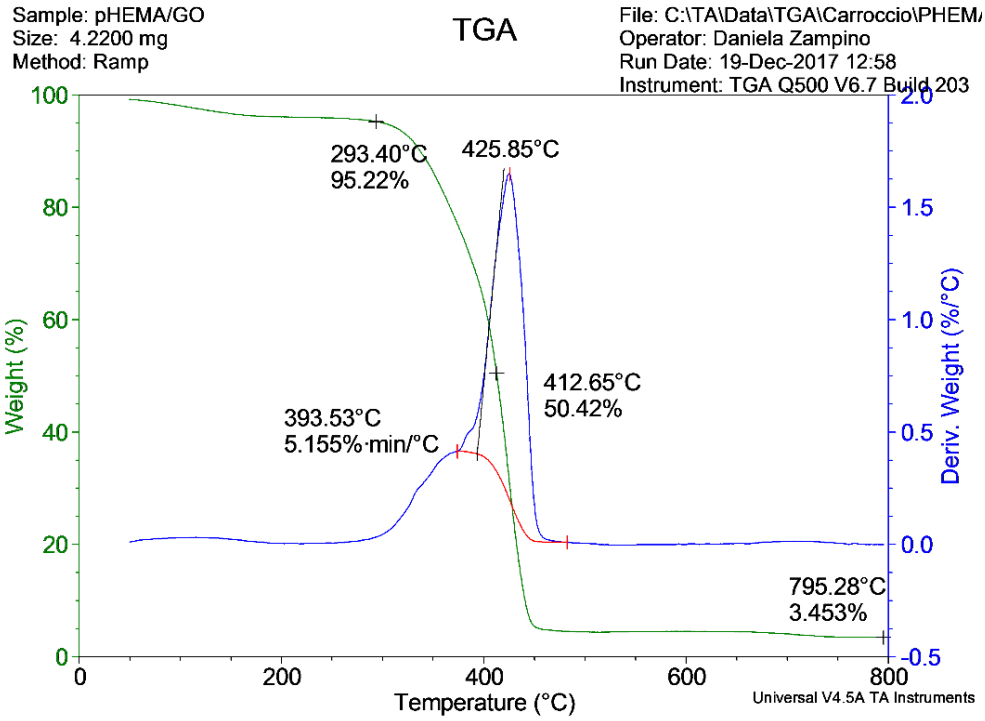

Figure S2. TG and DTG profiles of PHEMA/GO sample.

124x92mm (220 x 220 DPI)

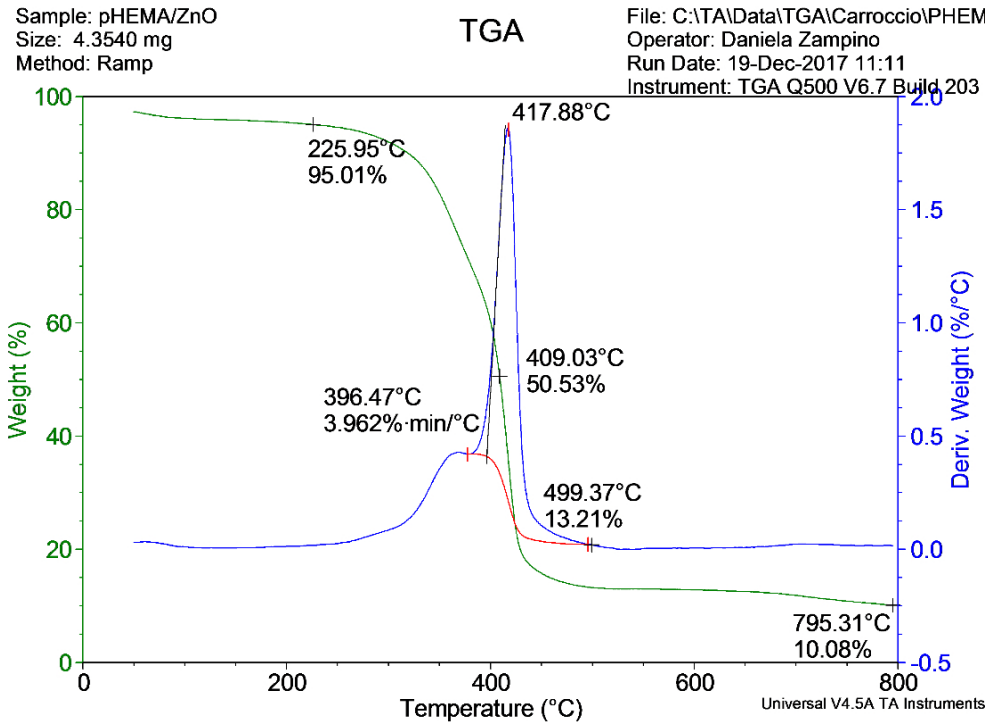

Figure S3. TG and DTG profiles of PHEMA ZnO sample.

129x95mm (220 x 220 DPI)

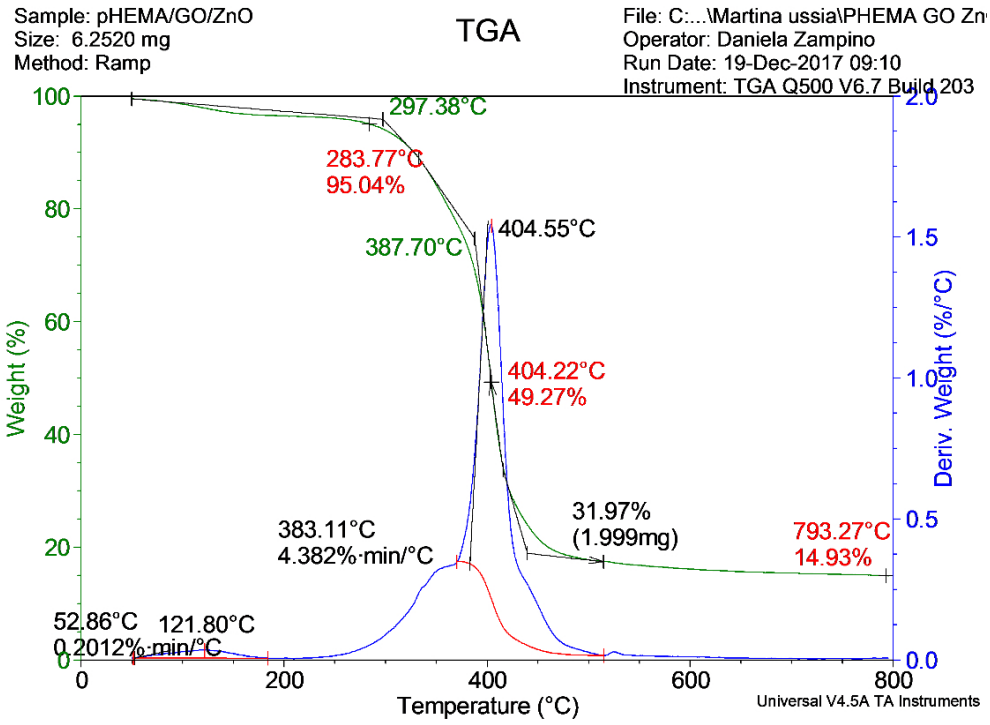

Figure S4. TG and DTG profiles of PHEMA/GO ZnO sample.

130x96mm (220 x 220 DPI)

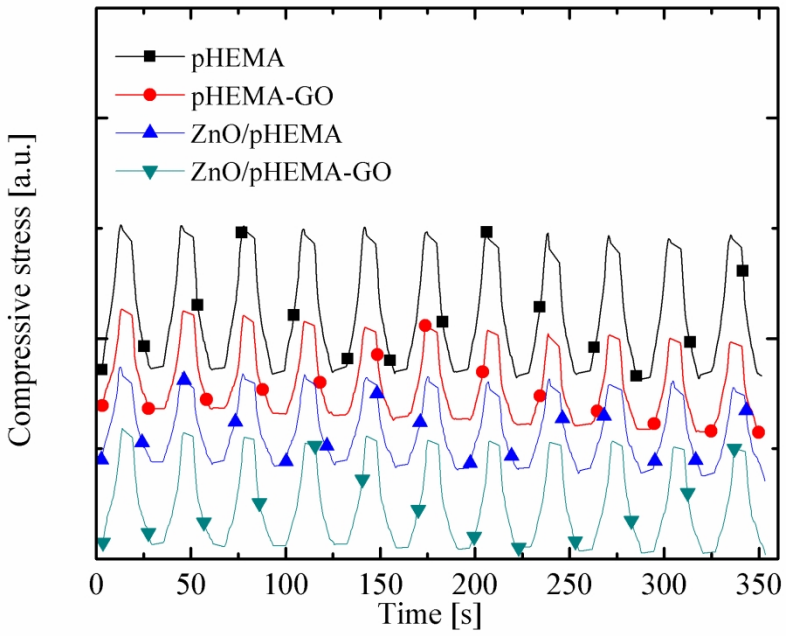

Figure S5. Compressive stress versus time curves of pHEMA, ZnO/pHEMA, pHEMA-GO, and ZnO/pHEMA-GO wet cryogels subjected to a 10-cycle compression test. The curves were vertically translated to improve readability.

201x154mm (300 x 300 DPI)

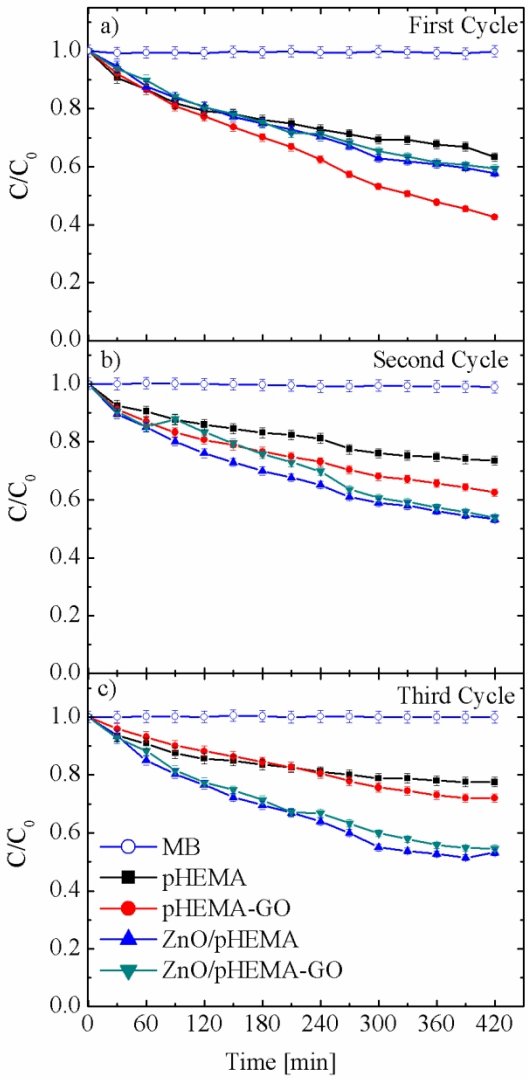

Figure S6. Three cycles of MB adsorption for pHEMA (squares), pHEMA-GO (circles), ZnO/pHEMA (up triangles), ZnO/pHEMA-GO (down triangles), and MB (open circles) as reference. In Y axis, C and C0 represent the MB concentration after t, and T0 adsorption times, respectively.

201x338mm (150 x 150 DPI)

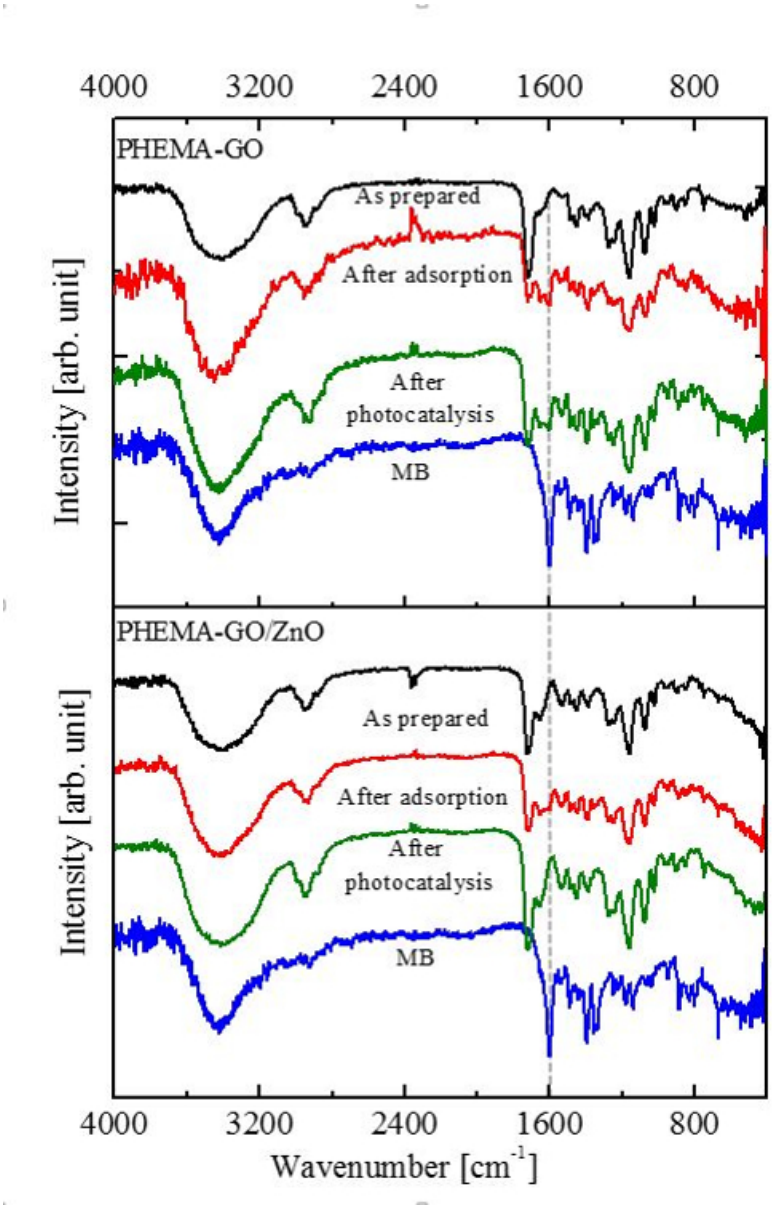

Figure S7. FTIR spectra measured on pHEMA-GO (a), and on ZnO/pHEMA-GO (b), as prepared (first spectrum from the top), after MB adsorption (second spectrum from the top), and after regeneration by UV light irradiation. The spectrum of pure MB is shown as reference. The spectra were vertically shifted for clarity. Vertical dashed lines indicate the typical stretching peak of MB.

129x190mm (100 x 100 DPI)

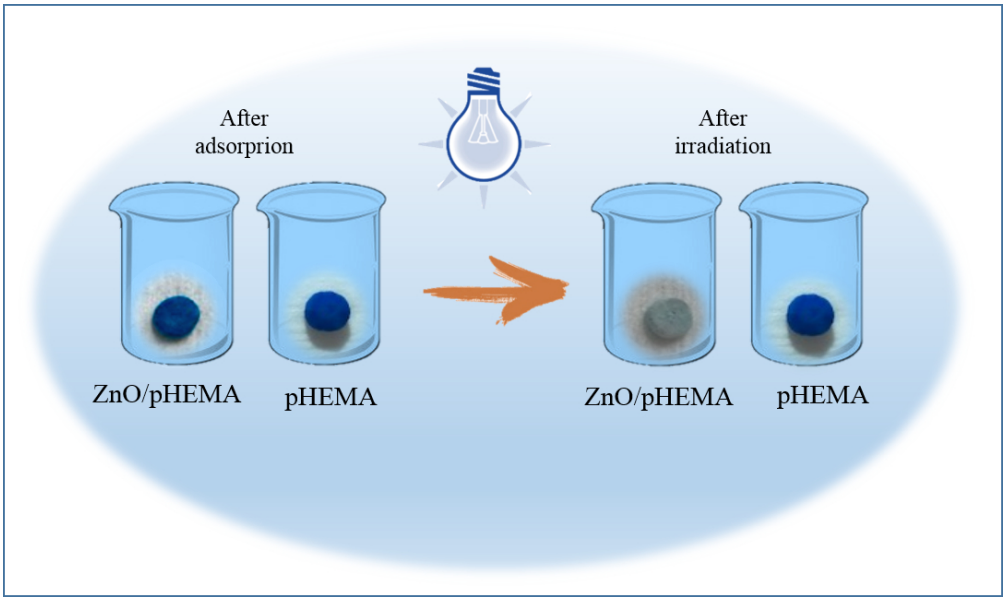

Graphical abstract

183x108mm (150 x 150 DPI)